# Modeling of Transient Photocurrent and Lag Signal in X-ray Imaging Detectors: Application to amorphous selenium

**Sinchita Siddiquee**

**A Thesis**

**in**

**The Department**

**of**

**Electrical and Computer Engineering**

**Presented in Partial Fulfillment of the Requirements for the Degree of Master of Applied Science (M.A.Sc) at**

**Concordia University**

**Montreal, Quebec, Canada**

**August 2015**

**CONCORDIA UNIVERSITY**
**SCHOOL OF GRADUATE STUDIES**

This is to certify that the thesis prepared

By:        Sinchita Siddiquee

Entitled:       "Modeling of Transient Photocurrent and Lag Signal in X-ray Imaging
                Detectors: Application to amorphous selenium"

and submitted in partial fulfillment of the requirements for the degree of

**Master of Applied Science**

Complies with the regulations of this University and meets the accepted standards with
respect to originality and quality.

Signed by the final examining committee:

_____ Chair
        Dr. R. Raut

_____ Examiner, External
        Dr. M. Mannan  (CIISE)                    To the Program

_____ Examiner
        Dr. H. Rivaz

_____ Supervisor
        Dr. M. Z. Kabir

Approved by:  _____
                    Dr. W. E. Lynch, Chair
            Department of Electrical and Computer Engineering

_____20_____                 _____
                                            Dr. Amir Asif, Dean
                                    Faculty of Engineering and Computer
                                                Science

# ABSTRACT

**Modeling of Transient Photocurrent and Lag Signal in X-ray Imaging Detectors: Application to amorphous selenium**

Sinchita Siddiquee

Flat-panel detectors (FPDs) are digital detectors that are widely utilised in medical applications such as general radiography and mammography. They are exposed to electromagnetic excitation to produce digital images of internal body organs. The electromagnetic radiation (optical or X-rays) creates electrons and holes in the photoconductor layer. These photogenerated electrons and holes drift under the influence of the applied electric field and constitute a photocurrent. Apart from the photocurrent, there is an undesirable current known as the lag signal detected in the devices after the removal of the excitation. The lag signal causes image artifacts in the digital image output that can lead to inaccurate or misleading medical diagnosis. Generally, the photocurrent and lag signals in FPDs are analyzed through experimental means. To the best of our knowledge, a complete mathematical model does not exist in literature to represent the entire current profile, which includes the photocurrent and the lag signal, for exponential carrier generation in FPDs.

This thesis is concerned with developing a mathematical model for transient photocurrent and lag signal in FPDs for X-ray and optical excitation by considering charge carrier trapping and detrapping in the energy distributed defect states under exponentially distributed carrier generation across the photoconductor. The model for the transient and

steady-state carrier distributions and hence the photocurrent has been developed by solving the carrier continuity equation for both holes and electrons. The lag signal is modeled by solving the trapping rate equations considering the thermal release and trap filling effects. The model is applied to amorphous selenium (a-Se) detectors for both chest radiography and mammography. The dependence of the lag signal on various factors such as X-ray exposure, applied electric field, and temperature is analyzed. The lag signal is found to be more prominent in chest radiographic detector than in mammographic detectors. Moreover, the transient rise and decay of the photocurrent profile as a function of time is studied. The quick rise and decay parts, and then the slow rise and decay parts of the photocurrent profile are due to the hole and electron transports, respectively. The model calculations are compared with the published experimental data and show a good agreement within the limits of experimental error. The satisfactory fittings of the experimental data with the model reveals the origin of the residual signal in the detector, which could be helpful for predicting the lag signal and designing the readout circuit and finding the ways to reduce lag.

# ACKNOWLEDGEMENT

I would like to express my deepest gratitude and appreciation to my thesis supervisor Dr. Zahangir Kabir for his guidance, encouragement and financial support throughout the progress of the work. Without his constant help and supervision, completing this thesis would not have been possible.

I would like to sincerely thank Salman Moazzem Arnab for many helpful discussions and suggestions. I am also grateful to other members of my research group including Nour Hijazi and Mesbahus Saleheen.

Finally, I would like to thank my parents, Dr. Habib Ibrahim Siddiquee and Mrs. Shaila Akhter, for their continuous support and for always being so actively engaged in every aspect of my life. And a very special thanks to my best friend and younger sister, Lamia Siddiquee, who has forever been my key emotional support.

**To**

**my parents**

**and**

**little sister**

# TABLE OF CONTENTS

# LIST OF FIGURES

# LIST OF TABLES

# LIST OF SYMBOLS

$\alpha$        attenuation coefficient

$\delta$        attenuation depth

$\varepsilon_0$        absolute permittivity

$\varepsilon_r$        relative permittivity

$\rho$        density

$\eta$        photogeneration efficiency

$\eta_q$        quantum yield

$\lambda$        wavelength of light

$\phi(F)$        field-dependent barrier potential

$\phi_0$        photon fluence

$\tau_h$        hole lifetime

$\tau_e$        electron lifetime

$\tau_c$        carrier capture time

$\tau_r$        carrier release or detrapping time

$\mu_h$        effective hole mobility

$\mu_e$        effective electron mobility

$v_0$        attempt-to-escape frequency

$C_t$        capture coefficient

$e$        electronic charge

$E_g$        mobility gap

$E_c$        conduction band edge

$E_v$        valence band edge

$E_{ph}$     energy of a photon

$F$     applied electric field

$g_h$     effective density-of-states at the valence band edge

$g_e$     effective density-of-states at the conduction band edge

$G_0$     carrier generation rate at $x = 0$

$I_0$     light intensity at $x = 0$

$J_h$     hole current density

$J_e$     electron current density

$J_p$     photocurrent density

$J_r$     residual current density

$k$     Boltzmann's constant

$L$     photoconductor length

$n(x,t)$   free electron concentration

$n_t(x,t)$   trapped electron concentration

$N(E)$   energy distributed density-of-states

$p(x,t)$   free hole concentration

$p_t(x,t)$   trapped hole concentration

$t$     time

$t'$     time after removal of excitation

$T$     absolute temperature

$T_{ex}$     exposure time

$V$     applied voltage

$X$     X-ray exposure

$x$     distance along the photoconductor

$W_\pm$    electron-hole pair creation energy

# LIST OF ACRONYMS

a-Se            amorphous selenium

a-Si:H          hydrogenated amorphous silicon

AMA             active matrix array

CR              computed radiography

DOS             density-of-states

EHP             electron-hole pair

FPD             Flat panel detector

ITO             indium tin oxide

IVAP            intimate valence alternation pair

keV             kilo electron-volt

TFT             thin-film transistor

TOF             time-of-flight

VAP             valence alternation pair

# CHAPTER 1: INTRODUCTION

## 1.1 Background

Flat-panels detectors (FPDs) are digital imaging detectors that are widely used in general radiography and mammography [1, 2]. They were first introduced towards the end of 1995 and have since played an important role in medical diagnosis and treatment. During medical imaging, the required body part is placed in front of the detector and exposed to X-rays. The X-rays that penetrate the body part are attenuated before it reaches the detector where they are converted to electric charges. The photogenerated charge carriers are henceforth collected by the active matrix array to produce the image output. The attenuated X-rays represent the lighter (white) portions of the X-ray image whereas the unattenuated radiation produces the darker sections.

There are two types of FPDs namely indirect and direct detectors. In indirect detectors, the X-rays are firstly converted to visible light and then to electric charges. In direct detectors, the X-rays are directly converted to electric charges in one step using a photoconductor [3]. The chalcogenic semiconductor, amorphous selenium (a-Se), is commonly used as photoconductor in direct FPDs [4]. In this thesis, amorphous selenium direct and indirect flat-panel detectors will be considered.

The electric charges created by the X-rays induce a photocurrent in the external circuit of the detectors. The magnitude of the photocurrent increases with the X-ray exposure as the carrier photogeneration is higher. Ideally, the photocurrent is supposed to flow as long as the device is exposed to the radiation. In reality, however, an exponentially decaying

current known as the residual current is detected for hundreds or thousands of seconds after the exposure is removed [5, 6]. The semiconductors (a-Se in this case) in the detectors have structural defects that act as traps. The defects appear as energy distributed localized density-of-states in the mobility gap of a-Se. The defects repeatedly capture and release carriers as they drift along the photoconductor. Depending on the depth from the mobility edge, the carrier release time of the defects varies along the mobility gap [7]. The deep traps found towards the center of the gap have very long release time, much greater than the average carrier transit time. This gives rise to the residual current in a detector. Since the modern day FPDs have a short time interval between successive exposures, the residual current from one exposure often interferes with subsequent exposures leading to image artifacts such as image lag [8]. Image lag often has serious consequences such as ambiguous and misleading results during medical diagnosis.

## 1.2 Photocurrent Analysis in Flat-panel detectors

The existence of the residual current has been known by researchers for a long time. Residual current is also known as lag signal or post-transit current. Several research groups have been performing the photocurrent analyses in a-Se detectors using mainly the time-of-flight (TOF) technique [9, 10, 11]. The TOF technique uses an ultra-short light pulse (mostly visible light) for photocurrent mapping [12]. For example, Benkhedir et al [13] used the post-transit TOF transients to study the density-of-states (DOS) distribution up to 0.53 eV below the conduction band edge. Instead of using only the post-transit current, Emelianova et al [10] used the entire current profile based on the TOF experiment to obtain reliable values of localized states in a-Se. A complete set of experimental data at various

electric fields and temperatures were fitted with a reference theoretical DOS model to obtain the energy distributed DOS values in a-Se.

Rau et al [14] developed a mathematical model based on the X-ray time-of-flight (TOF) technique to analyze ghosting in a-Se X-ray detectors. Considering uniform carrier generation across the semiconductor, Rau and colleagues developed expressions for free hole concentration and hole photocurrent in rested and ghosted a-Se detectors. The expressions were derived by solving first-order differential continuity equation for holes using appropriate limits. Considering a uniform carrier generation might not be a valid assumption for a lot of applications. Most medical applications such as radiography and mammography use X-rays in the keV range which are exponentially attenuated along the photoconductor. As the carrier generation follows the X-ray attenuation profile, considering an exponentially decaying carrier generation while developing the model is more reasonable. Moreover, their model is only valid for a very short pulse irradiation (the irradiation time being much shorter than the carrier transit time). Thus, this model does not apply to long pulse irradiation which is the case in mammography or chest radiography. In addition, lag signal was not considered in the model.

## 1.3 Research Objective

As mentioned earlier, lag signal can significantly affect image quality by introducing artifacts such as image lag. However, to the best of our knowledge, there are no mathematical models to represent the lag signal in FPDs. Therefore, this thesis is aimed towards developing a model for the entire current profile, which includes the photocurrent and lag signal, in a-Se direct detectors for long light and X-ray pulses. The carrier

generation will be considered to be exponentially decaying. Expressions for free carrier concentration, transient and steady-state photocurrent, trapped carrier concentration and residual current will be developed using physics based concepts and theories such as the Ramo-Shockley Theorem. Since the linear attenuation coefficient of light is much higher than X-rays, light is absorbed very close to the photoconductor surface. The photogeneration and induced current behavior for X-rays and visible light will be rather different. Hence two sets of equations, one for X-rays and the other for light, will be developed.

The dependence of the carrier concentration and residual current on conditions such as temperatures, electric field and so on will be quantitatively analyzed using the model. Moreover, the validity of the models will be verified by comparing them with published experimental data.

## 1.4 Contributions

The mathematical model for X-ray excitation in a-Se imaging detectors was developed to obtain expressions for carrier concentration and photocurrent by solving the space and time dependent continuity equations and for the residual current by solving the trapping rate equation. The model was applied to common medical applications namely chest radiography and mammography to analyze the results. This work has already been published in the following peer-reviewed journals and conference. This thesis work results the following:

- Sinchita Siddiquee and M. Z. Kabir, "Modeling of photocurrent and lag signals in amorphous selenium x-ray detectors," *J. Vac. Sci. Technol. A*, vol. 33, pp. 041514, 2015 [57].

- Sinchita Siddiquee and M. Z. Kabir, "Modeling of transient photocurrent in X-ray detectors: application to a-Se," *Physica Status Solidi* – under review [58].

- Sinchita Siddiquee and M. Z. Kabir, "Modeling of transient photocurrent in X-ray detectors: application to a-Se," *11$^{th}$ International Conference on Excitonic and Photonic Processes in Condensed Matter and Nano Materials,* Polytechnic Montreal, Canada, May 18-22, 2015.

Another mathematical model was developed for a-Se imaging detectors for optical irradiation. The results were plotted for analysis and the model was verified by fitting with published experimental data. A manuscript is under preparation for journal publication.

- Residual Photocurrent in amorphous selenium imaging detectors for Optical Excitation – under preparation.

## 1.5 Organization of the Thesis

The thesis is organized as follows:

Chapter 2 provides some background knowledge required to understand the work undertaken in this thesis. Firstly, the operating principles of flat-panel imaging detectors and the physical and carrier transport properties of amorphous selenium are explained.

Following that, the photocurrent behavior in a-Se imaging detectors and image lag artifacts are described.

In Chapter 3, a mathematical model for the transient photocurrent and lag signal in a-Se imaging detectors for X-ray and optical exposure is developed. The model is developed for an exponential carrier generation profile in the photoconductor. Expressions for free and trapped carrier concentration, transient photocurrent, photocurrent decay after removal of exposure and residual current are obtained by solving the carrier continuity equation. At first, a model for X-ray exposure is developed and then one for optical exposure is developed. Since the linear attenuation of light is much higher than X-rays, the optical model will be modified by considering some valid assumptions.

Chapter 4 shows the results obtained from the theoretical model proposed in the previous chapter. It will be analyzed how the free electron and hole concentration varies with carrier lifetime. The dependence of the residual current of various operational conditions such as ambient temperature, applied electric field and so on is also studied. Moreover, the electron and hole current contribution in the photocurrent decay current after removal of exposure will be analyzed. To verify the validity of the model, the theoretical results will be fitted with published experimental data.

Chapter 5 concludes this thesis by summarizing the main contributions made in this thesis, and suggesting some future work that can be undertaken along ideas and schemes presented in this thesis.

# CHAPTER 2: BACKGROUND CONCEPTS

## 2.1 Introduction

An overview of the background knowledge essential to understand the development of this thesis work is provided in this chapter. The basic operating principles of flat-panel detectors, the physical and carrier transport properties of amorphous selenium, the photocurrent behavior in amorphous selenium detectors and some other relevant topics are discussed.

## 2.2 Flat-Panel Detectors (FPDs)

The discovery of the X-rays in 1895 by Wilhelm Röntgen opened the pathway for medical imaging technology. The basic idea of obtaining images of internal body organs by exposing them to electromagnetic radiation, such as X-rays, for medical diagnosis has been employed time and again to produce an array of imaging techniques starting from 1900s. The earliest imaging devices exposed patients to the danger of high radiation dose but produced very low quality images. Years of research and development resulted in the modern day digital systems that can perform their operations within milliseconds and therefore protect patients from unnecessary radiation exposure [15]. Digital imaging detectors such as the flat-panel detectors are widely used today for commercial general radiography and mammography. Although there are flat-panel detectors under consideration that can complete its image readout process in ~1/30 s and hence applicable to real-time imaging techniques such as fluoroscopy, it has not yet been used commercially [16]. Figure 2.1 below shows a direct conversion digital mammography flat-panel detector

produced by Anrad Corporation. They are equipped with an active matrix array that helps produce a digital image on a computer shortly after a medical examination.



Figure 2.1: A direct conversion digital mammography flat-panel detector from Anrad Corporation [17].

Flat-panel detectors (FPDs) were brought into the market in the middle of 1995. Unlike cassette-based computed radiography (CR) systems, FPDs have built-in direct read-out electronics which make the devices slim and more convenient for usage. When X-rays are incident on FPDs, the radiation is absorbed and used to photogenerate electron-hole pairs (EHPs) [18, 19]. The back electrode responsible for charge collection is a pixelated active matrix array which is scanned row by row using peripheral electronics to read out the charges. The amount of charge collected from a particular pixel is proportional to the

radiation intensity received by the pixel. The collected charges finally produce the digital images which can be viewed almost immediately on a computer screen. Depending on the mechanism used to convert the X-rays to electric charge, FPDs can be broadly classified into indirect and direct detectors. Figure 2.2 below shows the mechanisms employed by direct and indirect detectors to produce image charges.
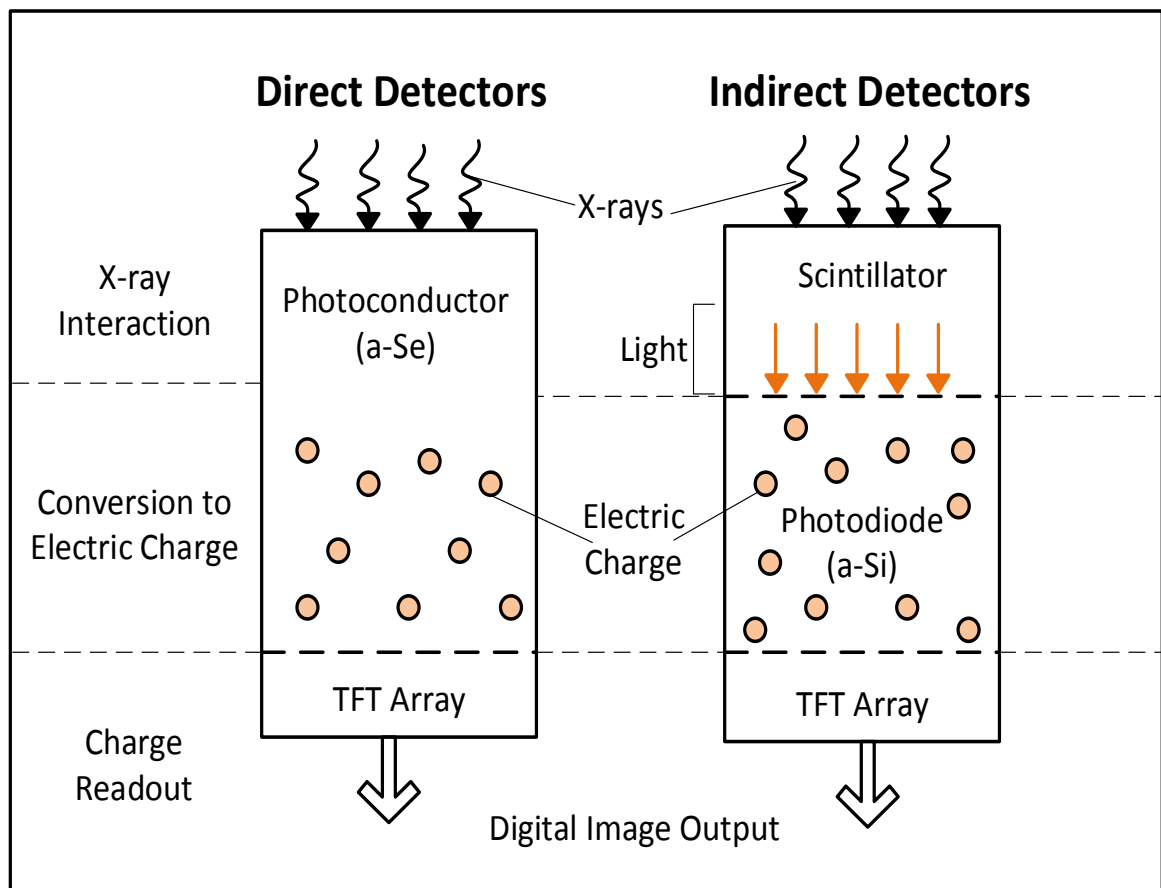


Figure 2.2: Operational mechanism of indirect and direct flat-panel imaging detectors. Direct detectors convert X-rays to electric charge directly using a photoconductor. Indirect detectors convert X-rays to visible photons using a scintillator and then transform the photons to electric charges using a photodiode. The latent charges are collected by the active matrix array to produce a digital image output [3].

Indirect detectors employ a two-step process whereby they firstly transform X-rays to visible light before converting them to electric charges using a photodiode. On the other hand, direct detectors directly convert X-rays to electric charges in one step using a photoconductor [20].

## 2.2.1 Indirect Detectors

Indirect detectors are flat-panel detectors that firstly convert the incident X-rays into visible light using a scintillator or phosphor screen and then use a p-i-n photodiode to convert the light to electric charges. A typical indirect detector structure consists of a scintillator or phosphor screen followed by a photodiode made of a sandwich structure consisting of layer of transparent indium tin oxide (ITO), a 10 to 20 nm thick $p^+$ blocking, a 1.5 μm thick intrinsic hydrogenated amorphous silicon (a-Si:H) and a 10 to 50 nm thick $n^+$ blocking layer. The bias voltage is applied to the detector through the ITO contact. Recently, a-Se detectors at extremely high fields (at avalanche mode) for light detection are under consideration for low dose X-ray imaging.

It has been observed that the spatial resolution of the image is reduced in indirect detectors due to the lateral scattering of light in the scintillator [3]. Although structured scintillators, which restrict the diffusion of light, were introduced to improve the image quality, it was found that the contrast and resolution in direct detectors are superior to their indirect counterparts.

## 2.2.2 Direct Detectors

Direct detectors possess better spatial resolution and signal-to-noise performance compared to indirect detectors which make them more suitable for medical applications like mammography [21]. Direct detectors have a simpler structure consisting of a bulk photoconductor that is electroded at both ends. The incident X-rays are converted to electron-hole pairs in one direct step in the photoconductor. An electric bias is applied across the structure through the electrodes which makes the electrons and holes drift in opposite directions perpendicular to the surface along the electric field lines without much lateral diffusion and loss of spatial resolution [22]. The metal/a-Se interfaces are blocking contacts which prevent carrier injection into the photoconductor but allow the X-ray generated carriers to be collected through the electrodes [23]. This reduces the noise due to dark current in the device.

Figure 2.3 below shows a positively-biased direct flat-panel detector setup where the electrons move towards the radiation-receiving electrode and holes drift to the pixelated back electrode. The latent charge distribution on the pixels are collected by the external electronics, digitized and sent to a computer for image processing.
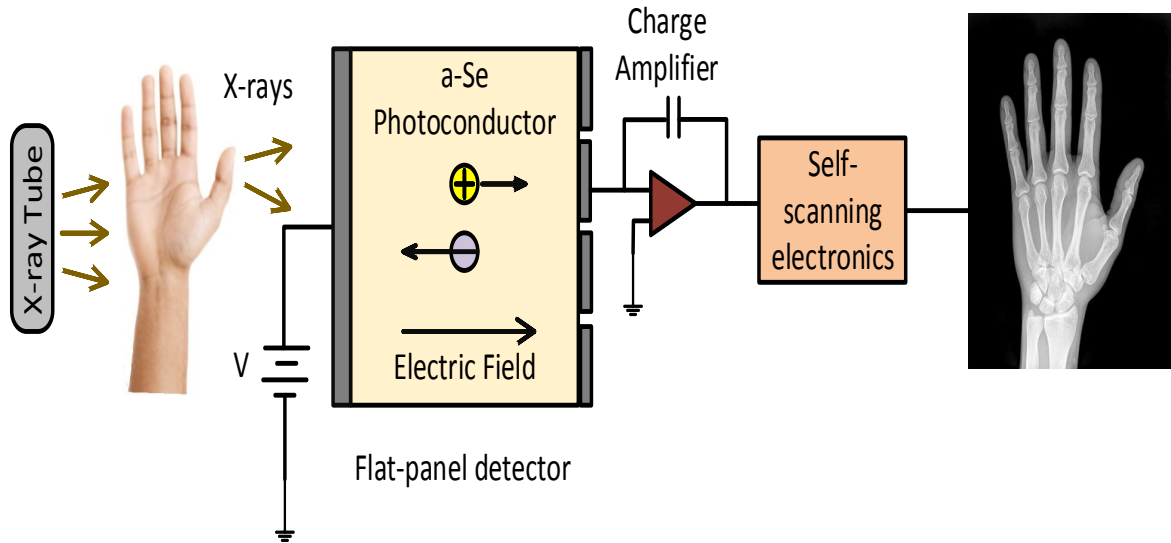
Figure 2.3: An X-ray imaging system consisting of a digital direct flat-panel detector. X-rays are absorbed in the a-Se photoconductor to generate EHPs which drift in opposite directions due to the applied electric field. For positive bias, the electrons are collected by the radiation-receiving electrode and the holes are collected by the active matrix array. The collected charges are amplified and digitized before being sent to a computer for the image output.

## 2.2.3 Active Matrix Array

The active matrix array (AMA) is a large-area integrated circuit that consists of millions of identical semiconductor devices that is used in FPDs, both direct and indirect, for charge readout [24]. Typically, FPDs use hydrogenated amorphous silicon thin-film transistor (a-Si:H TFT) active matrix array in their structure [25]. Each pixel electrode has a storage capacitor and TFT attached to it as shown in Figure 2.4 below.
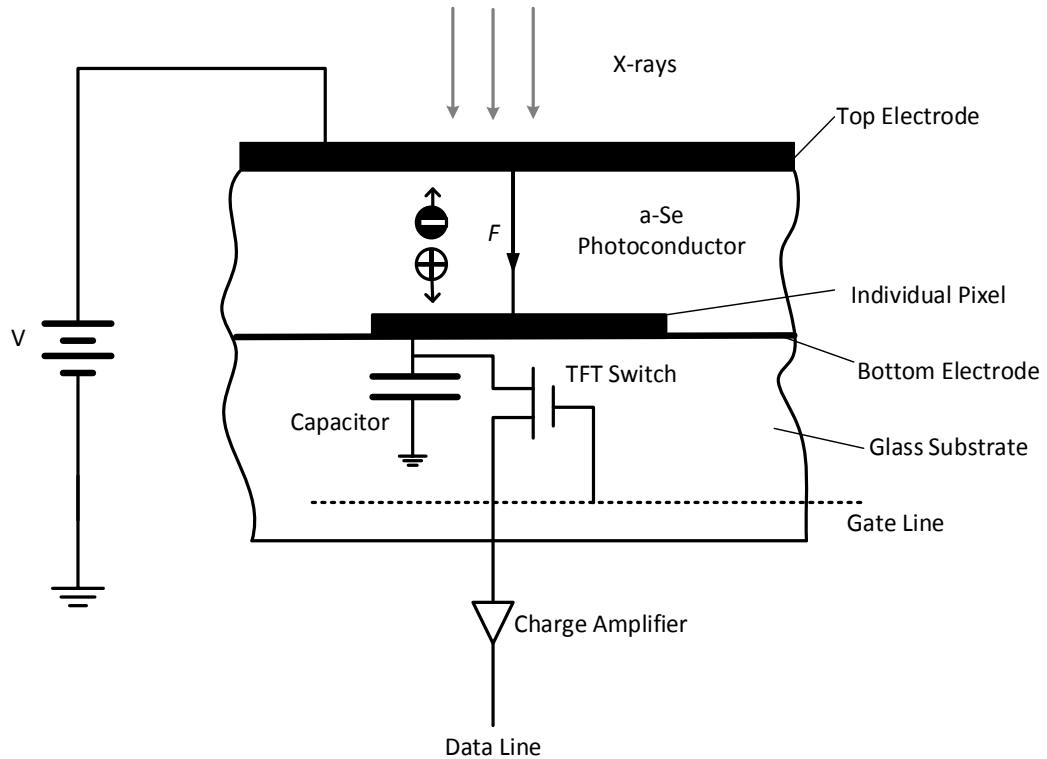
Figure 2.4: A simplified schematic diagram of the cross-sectional structure of a single pixel in an X-ray imaging detector [20]. Each pixel is attached to a capacitor and thin-film transistor (TFT) switch. The capacitor stores the latent charge until the particular gate line signal is turned on [4].

When electric charges reach a pixel electrode, they are stored in the capacitor. The TFT acts as a switch which conducts the charges to the data line only when the gate line signal for the required TFT is turned on. The active matrix readout takes place row by row. External self-scanning electronics and softwares control the state of the TFT switches by determining which gate line should be high at a particular time. Once the gate signal is high, the TFT switch conducts and allows the latent charge to be transferred to the data line.

From the data line, the charges are moved onto a charge amplifier and then to a multiplexer for parallel to serial data conversion. An analog to digital converter (ADC) digitizes the serial data to be used for image processing in a computer. Since the image processing time of FPDs is very fast, the image output can be obtained within seconds after the radiographic examination. The process is shown in Figure 2.5 below.
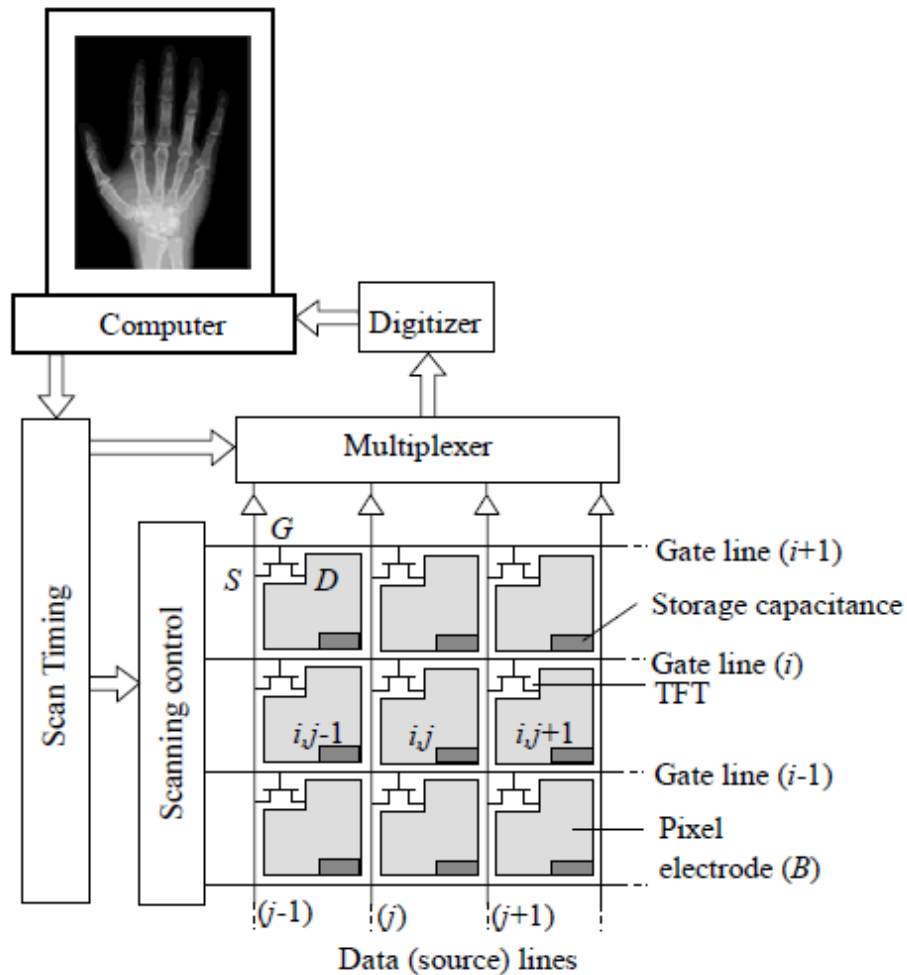


Figure 2.5: Schematic diagram showing few pixels of active matrix array (AMA) for use in X-ray imaging detectors with self-scanned electronic readout. The charge distribution residing on the panel's pixels are simply read out by scanning the arrays row by row using the peripheral electronics and multiplexing the parallel columns to a serial digital signal [20].

## 2.3 Clinical Applications of Flat-Panel Detectors

Digital detectors are used for a wide range of medical applications such as general radiography, mammography, fluoroscopy, angioscopy and so on. Currently, flat-panel detectors are commercially available for general radiography and mammography. FPDs suitable for fluoroscopy are still under the development phase. The size and properties of a detector depends on the particular application for which it was designed. For example, mammographic examinations involve imaging of soft breast tissues and, therefore, mammographic detectors require a higher spatial resolution and contrast compared to radiographic detectors. Table 2.1 shows the typical device requirements for various medical examinations [26].

| Clinical Task | Chest Radiography | Mammography | Fluoroscopy |
|---|---|---|---|
| Detector size | 35 cm × 43 cm | 18 cm × 24 cm | 25 cm × 25 cm |
| Pixel size | 200 μm × 200 μm | 50 μm × 50 μm | 250 μm × 250 μm |
| Number of pixels | 1750 × 2150 | 3600 × 4800 | 1000 × 1000 |
| Readout time | ~ 1 s | ~ 1 s | 1/30 s |
| X-ray spectrum | 120 kVp | 30 kVp | 70 kVp |
| Mean exposure | 300 μR | 12 mR | 1 μR |
| Exposure range | 30 – 3000 μR | 0.6 – 240 mR | 0.1 – 10 μR |

Table 2.1 Requirements for Digital X-ray imaging systems for different medical applications

## 2.4 Photoconductors for Direct Detectors

Photoconductors play a key role in the operation of flat-panel detectors. The structure and carrier transport properties of the photoconductor determine the sensitivity, resolution and quantum efficiency of the detector and hence affect the overall performance of the detectors. A photoconductor is required to have the following properties:

(i)     A photoconductor must have a high attenuation coefficient so that the attenuation depth of the X-rays, $\delta$, is substantially less than the photoconductor length, $L$.

(ii)    The electron-hole pair (EHP) creation energy, $W_\pm$, of a photoconductor should be as small as possible. The value of $W_\pm$ usually depends on its bandgap $E_g$.

(iii)   The dark conductivity of a photoconductor should be negligible as dark current is a source of noise in the detectors.

(iv)    A photoconductor should be convenient for large-area coating on the active matrix array (AMA) of the detector without raising the substrate temperature to damaging levels.

(v)     A photoconductor should have uniform characteristics over the entire area and the characteristics should not change with time and repeated radiation exposure.

As we know, there are three basic types of solids: crystalline, polycrystalline and amorphous. They have different atomic arrangements as shown in Figure 2.6. Crystalline solids are long range materials that have a uniform atomic arrangement throughout its structure. Polycrystalline solids consist of a group of crystals with different orientations

16

combined together to form a single solid. The boundary between two different crystal structures is known as a grain boundary. Amorphous solids have very short range order. The atoms in their structure are randomly arranged with different bond lengths and bond angles.

Grain Boundary

Disordered Arrangement

atoms

(a) Crystalline

(b) Polycrystalline

(c) Amorphous
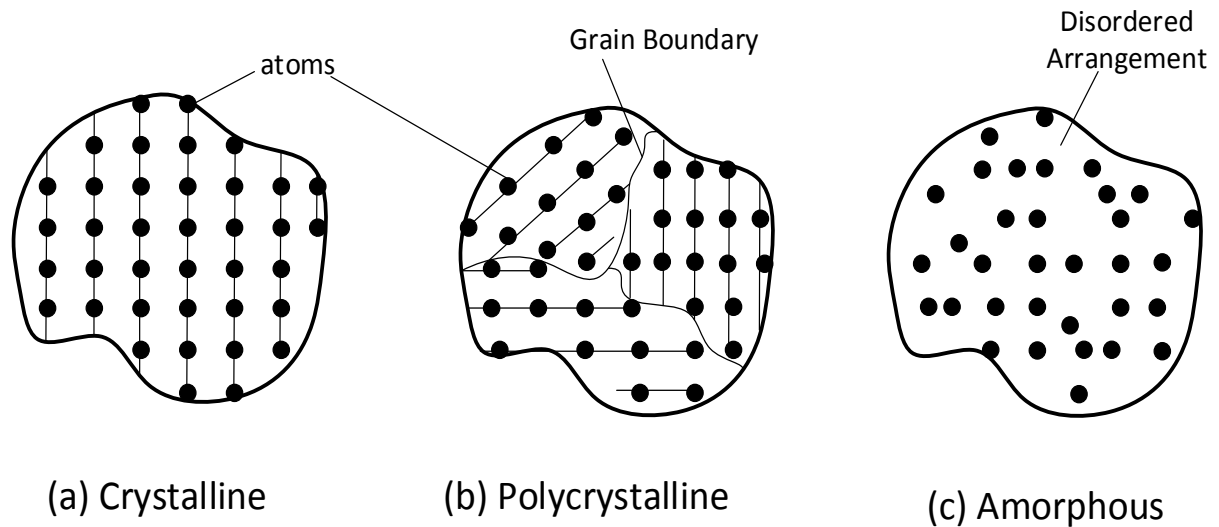
Figure 2.6: Three types of solids based on their atomic structural arrangement. Crystalline solids have uniformly arranged atoms throughout its structure (long-range order). Polycrystalline solids consist of small uniformly arranged crystals (also known as grains) randomly combined together to form a single solid. Amorphous solids have very short-range order due to randomly arranged atoms with different bond lengths and angles.

Most FPDs require a large area photoconductor coating of about 30 cm × 30 cm or greater without raising the substrate temperature to damaging levels (beyond 60 – 70 °C) for the AMA. Due to their structural properties, crystalline semiconductors are difficult to deposit on large areas while maintaining the required temperature range. That is why

polycrystalline and amorphous solids are the preferred choice for photoconductors. Polycrystalline semiconductors such as $Cd_xZn_{1-x}Te$ (CZT), $HgI_2$, $PbI_2$ and PbO and amorphous semiconductors such as a-Se, $a-As_2Se_3$, a-Si:H, etc. are commonly used as photoconductors in imaging detectors. The grain boundaries in polycrystalline structures, however, tend to limit their charge transport properties. As a result, amorphous materials are more extensively used as photoconductors. Amorphous selenium (a-Se) is the most common photoconductor found in direct FPDs. Initially, it gained popularity in the 1960s for its xerographic applications but was later replaced by cheaper and more efficient organic compounds [4]. It regained its popularity back around 1980s due to the introduction of the FPDs and has since been playing a key role in medical imaging applications.

## 2.5 Amorphous Selenium (a-Se)

Despite the introduction of several photoconductor materials over the years, amorphous selenium (a-Se) has been the most widely used photoconductor for flat-panel X-ray detectors for almost three decades. The relative ease with which a-Se can be deposited by conventional vacuum deposition technique over large areas of the AMA without raising the substrate temperature above 60 – 70 °C has been one of the key reasons behind its popularity. In addition, excellent X-ray absorption properties, good charge transport properties and low dark conductivity in a-Se make it an ideal photoconductor for most applications.

Pure a-Se is thermally unstable and crystallizes with time which makes it unsuitable for photoconductor applications. That is why various impurities are often added to it to

enhance its structural properties and charge transport behaviour. In 1966, Kolomiets and Lebedev investigated the dependence of a-Se sensitivity on the concentration of added impurities such as S, Te, P and so on [27]. Different elements were found to have different effect on the charge transport properties of a-Se. For example, adding Cl enhances hole range (modality × lifetime) but eliminates electron transport. Na, however, has the reverse effect; it enhances electron transport. Stabilized a-Se is formed by adding $0.2 - 0.5\%$ of the group III element Arsenic (As) to a-Se. As increases the viscosity of a-Se and slows down crystallization. However, As increases the number of hole traps and, consequently, reduces the hole lifetime in the amorphous semiconductor. $10 - 40$ p.p.m (parts per million) of Cl is usually added to a-Se to compensate the carrier transport effects of As. The nominal composition for stabilized a-Se is $0.3\%$ As $+ 20$ p.p.m Cl. The stabilized form of a-Se is used as photoconductor in imaging detectors [28].

Selenium belongs to the group VI column of the periodic table known as chalcogens. It has an atomic number of 34 with 6 valence electrons in its outer shell. The electronic structure of selenium is given by [Ar] $3d^{10}4s^24p^4$. Selenium can exist in either crystalline or amorphous form. In crystalline selenium (c-Se) the atoms are systematically arranged in a specified long-range order. In amorphous selenium (a-Se), the bond lengths and angles varies randomly to produce a structure with short range order. Normally, selenium is a divalent element, ie. each atom in its structure bonds with two other neighboring atoms. In a-Se, however, the individual Se atoms bond with other atoms to satisfy their valency, thus resulting in under-coordinated and over-coordinated bonding throughout its structure [29,30]. In under-coordinated bonds, the selenium atoms bond with only one other atom and in over-coordinated bonds, each atom bonds with three other atoms. The random

arrangement results in many structural defects in a-Se such as dangling bonds which play an important role in the physical and electrical properties of the material.

The lowest-energy neutral defect in a-Se is not the dangling bond but rather the threefold coordinated selenium atom $Se_3^0$. The dangling bonds are structural defects formed at the chain ends. They are singly coordinated atoms represented by $Se_1^0$. The superscript on each atom represents the charge on the atom and the subscript shows the number of atoms it is bonded to. A pair of charged defects $Se_3^+$ and $Se_1^-$ are called valence alternation pair (VAP). If they are in close proximity, they appear neutral overall and are called intimate valence alternation pair (IVAP) [31]. Since the localized DOS in a-Se is energy distributed, there are many other neutral defects in the mobility gap of a-Se whose exact nature are not yet well understood.

## 2.5.1 Density-of-States in a-Se

We know that isolated atoms possess quantized energy levels. But, according to the band theory of solids, as two atoms move close to each other, the quantized levels hybridize and split into two energy levels because of the mutual interaction of the two atoms. When N atoms are found in close proximity interacting with each other, the energy levels split into N levels. As N becomes very large, for example in a crystal solid, the levels move close to one another and eventually form a continuous energy band. In conductors, the conduction and valence bands overlap each other to facilitate the transport of valence electrons throughout the solid. Semiconductors, however, have a small energy gap, called a bandgap or mobility gap, between the conduction and valence bands. If we say that the energy at

bottom of the conduction band is given by $E_c$ and the energy at the top of the valence band is $E_v$, then the bandgap $E_g$ is given by $E_g = E_c - E_v$. This characteristic energy gap in semiconductors gives them some unique physical and transport properties. Electrons in the valence band of semiconductors need to acquire enough energy from thermal or electromagnetic excitation to reach the conduction band and be available for conduction.

Crystalline semiconductors possess energy states only above the conduction band and below the valence band and have an empty energy bandgap. Amorphous semiconductors (eg. a-Se) have an energy state distribution even in their mobility gap due the structural defects mentioned earlier. The defects appear as energy distributed localized density-of-states (DOS) in the mobility gap and act as trapping or recombination centers for charge carriers. To obtain the energy distributed density-of-states in a-Se, many researchers have employed various techniques such as time-of-flight photoconductivity measurements, xerographic measurements and post-transit photocurrent analysis [32]. However, despite continuous research since the 1970s, there remains disagreement about the exact shape of the localized states distribution in a-Se. In 1977, Owen and Marshall studied the charge transport properties in amorphous semiconductors and suggested the presence of localized states at various well-defined energies in addition to tail states. Later in 1988, Abkowitz [33] extended the Owen – Marshall model by using combined analysis of xerographic potentials and transient transport data to obtain a reliable DOS model for undoped and doped a-Se. The DOS distribution in a-Se according to the Abkowitz model is shown in Figure 2.7 below.
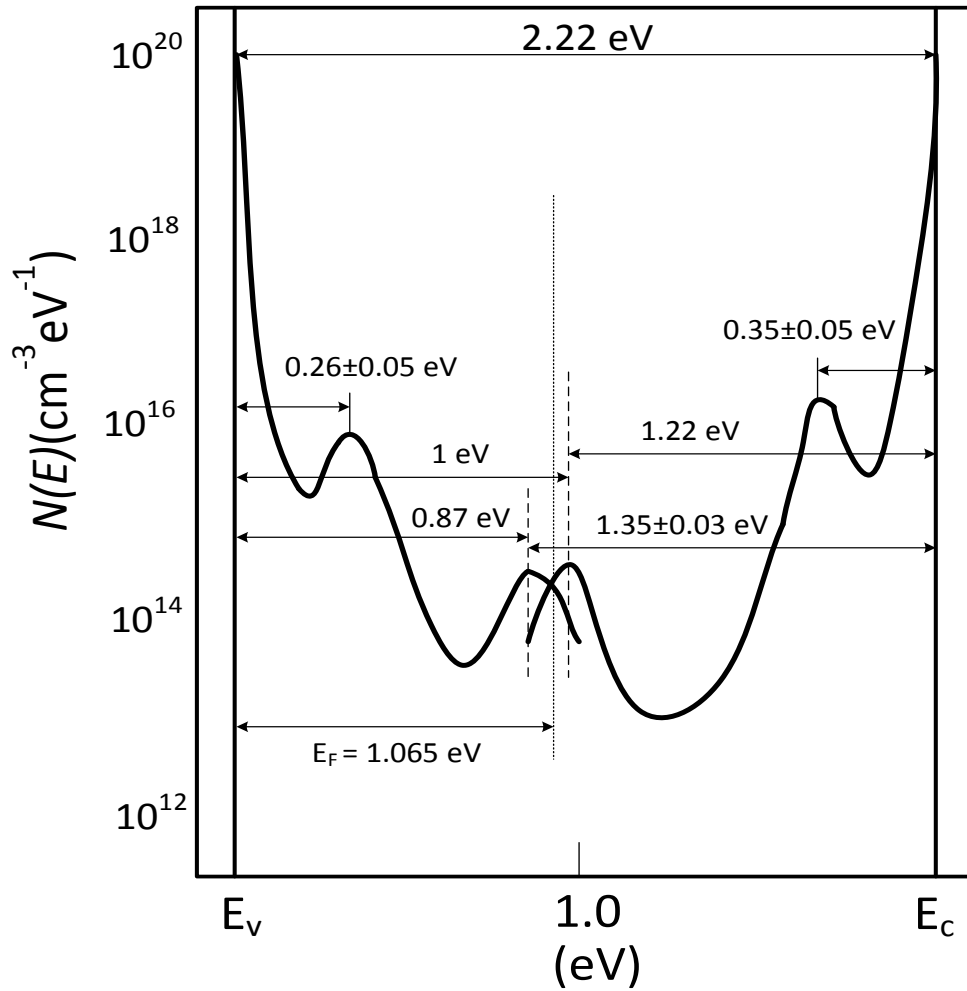
Figure 2.7: The localized density-of-states distribution in a-Se according to the Abkowitz model [33]. The exponentially decaying tail states and the Gaussian curves close to the mobility edge represent the shallow traps and the smaller Gaussian curves deep within the mobility gap represents the deep traps.

Essentially, the mobility gap in a-Se consists of two exponentially decaying tail states extending from the valence and conduction band edges and continuing into two narrow Gaussian curves. They represent the shallow traps in a-Se that capture the carriers for a small detrapping time and thus only alter the effective mobility of the carriers. The energy

states close to the valence band act as hole traps whereas the ones located near the conduction band act as electron traps. The peak of the Gaussian curve for shallow hole traps appear at about 0.26 eV below the valence band edge and that for electron traps appear at 0.35 eV below the conduction band edge. The exact position of the peak can vary for about ±0.05 eV depending on the fabrication technique, degree of doping impurities and the evaluation technique. There are two secondary smaller peaks found deep within the center of the mobility gap which are known as the deep traps. Due to their position, they have a very long carrier release time (much longer that the typical carrier transit time in detectors). For hole deep traps, the Gaussian curve is centered at about 0.87 eV below the valence band and, for electron deep traps, the curve appears at 1.22 eV below the conduction band. The magnitude of the shallow traps for both electrons and holes is about $10^{16}$ cm$^{-3}$eV$^{-1}$ whereas the magnitude for deep traps can vary anywhere between $10^{14}$ cm$^{-3}$ eV$^{-1}$ to $10^{15}$ cm$^{-3}$ eV$^{-1}$.

## 2.5.2 Photogeneration in a-Se

When an X-ray photon is absorbed by a material such as a-Se, the incident photon ionizes an atom to create a free high energy electron using the photoelectric effect. This primary electron then goes on to create many more EHPs along its way. The photoelectric attenuation coefficient α of any material depends on the energy $E_{ph}$ of the incident photons, the atomic number and the density of the material. The attenuation coefficient is inversely dependent on the photon energy. In other words, when a high energy photon strikes a photoconductor, the attenuation coefficient is much lower than that compared to lower energy photons. However, attenuation coefficient increases when the atomic number of the

material increases. We know that one of the key requirements when designing an imaging detector is minimum exposure dose to the patient. To achieve that, most of the radiation must be attenuated in the photoconductor length before it reaches the patient. Therefore, the penetration depth $\delta = 1/\alpha$ must be several times smaller than the photoconductor thickness (ie. $1/\alpha << L$).

Empirically, the attenuation coefficient of a-Se is related to the photon energy $E_{ph}$ by the expression [4]

$$\alpha \approx (6.67 \times 10^5) E_{ph}^{-2.7055} \tag{2.1}$$

Where $\alpha$ is in 1/cm and $E_{ph}$ is in keV. For mammography, for example, which has average photon energy of 20 keV, the penetration depth $\delta$ is about 48 µm. As a result, photoconductor length $L$ of 200 µm is sufficient for absorbing most of the radiation in mammographic examinations. But for chest radiography (60 keV), $L$ is taken to be about 1000 µm since the penetration depth $\delta$ is about 1 mm. A greater photoconductor length is not used for chest radiography since increasing the length beyond 1000 µm reduces the sensitivity of the detector due to poor charge collection efficiency [34].

The EHP creation energy denoted by $W_{\pm}$ is defined as the amount of incident radiation energy absorbed to create a single free electron-hole pair (EHP). In a-Se, it varies from about 35 to 55 eV for the diagnostic beam energy range of 12 to 120 keV for an applied electric field of 10 V/µm. It should be as small as possible for a material to have excellent photoconductivity. EHP creation energy is dependent on photon energy and electric field

but independent of temperature. In a-Se, it depends strongly on the applied field but has a weak dependence on X-ray photon energy [35, 36]. $W_{\pm}$ at a given $E_{ph}$ in a-Se follows an empirical relation given by

$$W_{\pm} \approx W_{\pm}^0 + \frac{B(E_{ph})}{F^n} \tag{2.2}$$

where $B(E_{ph})$ is a constant that depends on $E_{ph}$, $W_{\pm}^0$ is the saturated EHP creation energy (at infinite $F$), and $n$ is typically 0.7–1 [37]. The value of $W_{\pm}^0$ should be $2.2E_g + E_{phonon}$, where $E_{phonon}$ is the phonon energy. With $E_g \approx 2.22$ eV and $E_{phonon} < 0.5$ eV, we would expect that $W_{\pm}^0 \approx 5$–6 eV. The following empirical relation can be used to describe the electric field and energy dependence of $W_{\pm}$,

$$W_{\pm} = \left(6 + \frac{15 \times 10^6}{F^{0.8}}\right) \times \left(0.72 + 0.56 \times \exp(-E_{ph}/62700)\right) \tag{2.3}$$

One interesting point to note here is that not all of the photogenerated charges are collected at the electrodes. This is because the oppositely charged particles are attracted to each other by their Coulombic force and might eventually recombine. When the applied electric field is higher, the charges can more easily overcome the Coulombic attraction and be available for conduction. The photoconductive photogeneration efficiency $\eta$ is defined as the fraction of generated EHPs that escape recombination with respect to the total number of EHPs created in the photoconductor and is given by [34,38]

$$\eta = \frac{W_{\pm}^{0}}{W_{\pm}} \qquad\qquad (2.4)$$

where $W_{\pm}^{0}$ is the lowest or saturated EHP creation energy at infinite electric field and $W_{\pm}$ is the actual value of the parameter in the device. It has been observed that the photogeneration efficiency in amorphous semiconductors increases with increasing electric field.

## 2.5.3 Charge carrier transport in a-Se

It was seen in the previous sections how the material properties of the photoconductor play an instrumental role in the transport properties of the photogenerated carriers. In bulk amorphous selenium (a-Se), the transport of the holes and electrons are affected by the defect states found in its mobility gap. The repeated carrier capture and release by the traps affects the effective mobility of the carriers. As the name suggests, the capture time $\tau_c$ is the mean time before a carrier is trapped by a defect and the release or detrapping time $\tau_r$ is the mean time the carrier is trapped before being released to the extended states. Since shallow traps are located very close to the mobility edge, the carriers in shallow traps can easily be excited to the extended states. As a result, the detrapping time for these traps is very small. Release time for shallow trapped electrons is about 100 ns and, for holes, it is less than 100 ns. Generally, the shallow traps only alter the effective mobility of the carriers. Deeps traps, however, have a long detrapping time as they are found deep within the mobility gap. Their release time is comparable to the transit time in the detectors. Release time for deeply trapped holes is less than 10 minutes and for electrons it can be about a few hours or longer.

Figure 2.8 shows the transport of electrons and holes in the photoconductor under the applied electric field. Holes drift in the direction of the field and electrons drift in the opposite direction.
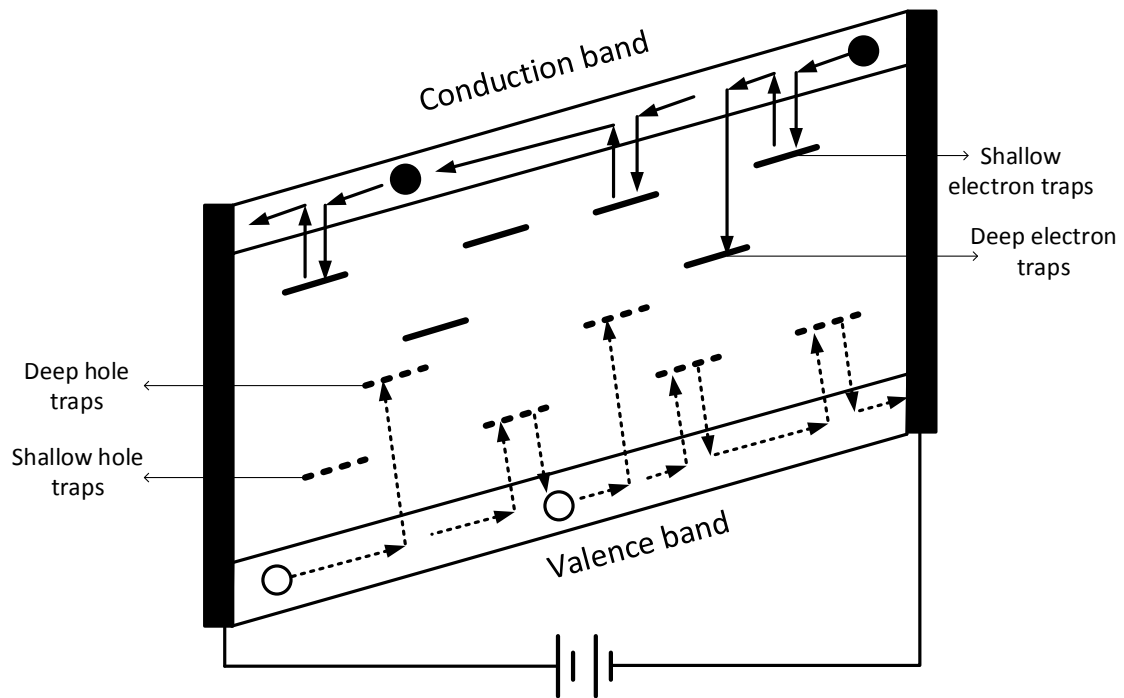


Figure 2.8: The drift of carriers in the photoconductor under the influence of electric field. The holes drift in the direction of the electric field whereas the electrons drift in the opposite direction. The carriers are trapped by shallow and deep traps along the way. The carriers are quickly released from the shallow traps due to their close proximity to the band edges. Deep traps, however, have a much longer release time [39].

The hole and electron mobility in the extended states is 0.3 and 0.1 cm$^2$/V-s respectively at room temperature [40,41]. The effective mobility, on the other hand, at room temperature is about 0.12 cm$^2$/V-s for holes and 0.003 – 0.006 cm$^2$/V-s for electrons. The carrier lifetime in semiconductors is closely related to the carrier capture time. Carrier lifetime depends on the concentration of deeps traps rather than shallow traps. In a-Se, the typical values of hole

lifetime is 20 – 200 µs and that for electrons is 200 – 1000 µs. Table 2.2 summarizes some of the transport properties of a-Se.

| Properties | Symbol | Value | Unit |
|---|---|---|---|
| **Density** | $\rho$ | 4.3 | g/cm |
| **Relative permittivity** | $\varepsilon_r$ | 6.7 | – |
| **Mobility gap** | $E_g$ | 2.2 | eV |
| **Effective hole mobility** | $\mu_h$ | 0.12 – 0.14 | cm$^2$/V-s |
| **Effective electron mobility** | $\mu_e$ | 0.003 – 0.006 | cm$^2$/V-s |
| **Hole lifetime** | $\tau_h$ | 20 – 200 | µs |
| **Electron lifetime** | $\tau_e$ | 200 – 1000 | µs |

Table 2.2 Important physical and transport properties of amorphous selenium.

Carrier schubweg is another important parameter in charge carrier transport. It is defined as the average distance a carrier drifts before it is deeply trapped and unavailable for conduction. It is given by the product of effective mobility, carrier lifetime and applied electric field (ie. schubweg = $\mu\tau F$). For both electrons and holes, the schubweg must be much greater than the photoconductor thickness $L$.

According to the multiple trapping model, the charges remain immobile when they are captured by the localized energy states and, hence, must be excited to the extended states above the mobility gap to allow conduction [42]. The release or detrapping time from the

traps is, therefore, a very important parameter. It can simply be defined as the time it requires for a trap to release a captured carrier. It is given by the formula

$$\frac{1}{\tau_{rh}} = v_0 \exp\left[-\left(\frac{E - \phi(F)}{kT}\right)\right]$$

(2.5)

where $v_0$ is the attempt-to-escape frequency and $\phi(F)$ is the field induced barrier lowering. Emission of trapped charges in an electric field is facilitated by three main mechanisms namely Poole-Frenkel effect, phonon-assisted tunneling and direct tunneling. Direct tunneling plays a part only when the electric field is extremely high at about $10^7$ V/cm. For lower electric fields, detrapping occurs via Poole-Frenkel mechanism or phonon-assisted tunneling which is also known as thermal tunneling.

The thermally activated tunneling mechanism applies when the unoccupied defect is neutral, while the Poole-Frenkel model applies when the unoccupied defect is a charged defect. The mechanisms are illustrated in Figure 2.9. There has been an ongoing debate over the state of deep traps being neutral or charged. A recent paper published by Berashevich et al [43] suggests that the deep traps (deeper than 0.5 eV) in a-Se are neutral traps. Since the deeper states (deeper than 0.5 eV) mostly control the residual current, the thermally-assisted tunneling mechanism has been considered in this paper. The shallower trap levels are unable to retain sufficient amount of trapped charges during irradiation because of faster release event [44].
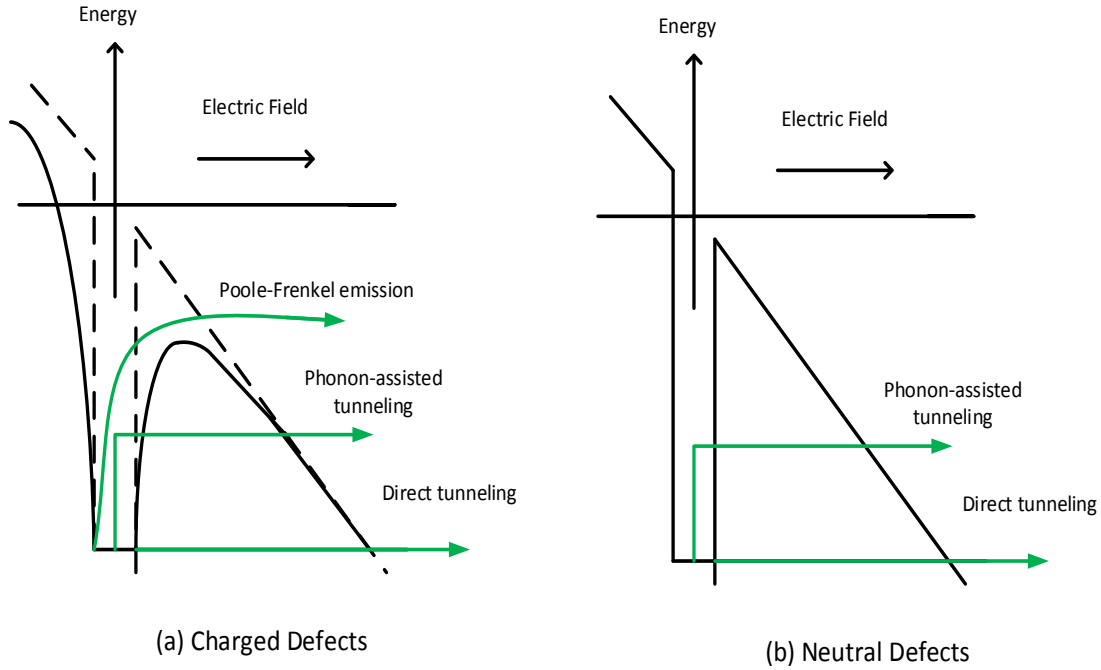
Figure 2.9: The carrier detrapping mechanisms in (a) charged defects and (b) neutral defects. Carrier release in charged defects occurs via Poole-Frenkel mechanism and phonon-assisted tunneling at low and high electric fields respectively. In neutral defects, phonon-assisted tunneling releases trapped carriers at all applied fields [45].

In Poole-Frenkel mechanism, the barrier potential is lowered due to the presence of the electric field which enables the carrier to easily overcome the height and become free for conduction. Initially, the Poole-Frenkel effect was analyzed in one dimension [46]. However, Hartke and Jonscher later extended the model for three-dimensional analysis which provides better agreement with experimental results [47, 48]. For one-dimensional Poole-Frenkel effect, the barrier lowering potential is given by

$$\phi(F) = \sqrt{eF/\pi\varepsilon_s} \tag{2.6}$$

where $\varepsilon_s = \varepsilon_0 \, \varepsilon_r$ is the permittivity of the material. For the three-dimensional Poole-Frenkel model,

$$\exp\left[\frac{\phi(F)}{kT}\right] = \left[\frac{1}{\gamma^2}\right]\left[e^\gamma (\gamma - 1) + 1\right] + \frac{1}{2} \tag{2.7}$$

where

$$\gamma = \left(\frac{eF}{\pi\varepsilon_s}\right)^{1/2} \frac{e}{kT} \tag{2.8}$$

In phonon-assisted tunneling, the carrier gains thermal energy to escape through a narrower barrier width. For this mechanism, the barrier lowering potential is given by

$$\phi(F) = aF \tag{2.9}$$

where $a$ is the effective tunneling distance along the field.

## 2.6 Photocurrent Analysis in FPDs

The basic operational principle of image detectors implies that when a detector is exposed to external irradiation, the current should instantaneously increase from zero to the maximum value (transient current). Then the detector should maintain the value for the duration of the exposure (steady-state current) until the radiation is taken away [49]. In reality, the picture is rather different.

A very small magnitude of current called the dark current flows in these detectors even when it is placed in the dark. The current is formed by thermally generated carriers. The dark current in detectors is tried to be kept at a minimum since it is a source of noise. The dark resistivity of a-Se is about $10^{14}$ $\Omega$-cm. The dark current in a-Se detectors is usually lower than the acceptable level of 1 nA/cm$^2$ even for an electric field as high as 20 V/$\mu$m.

The residual current, on the other hand, is detected after the exposure is turned off. Instead of returning to zero, the photocurrent decays for hundreds or thousands of seconds after the removal of the exposure. Localized defects states are believed to be responsible for residual current in detectors. Residual current is also known as the lag signal. It often causes an artifact in digital detectors known as image lag. Figure 2.10 below shows the typical dark and photocurrent decay after exposing an imaging detector to a long light pulse. It can be seen that there is an exponentially decaying dark current before the detector is exposed to light. When a pulse of light is radiated, the photocurrent reaches a peak and then decays as the residual current when the radiation is turned off.
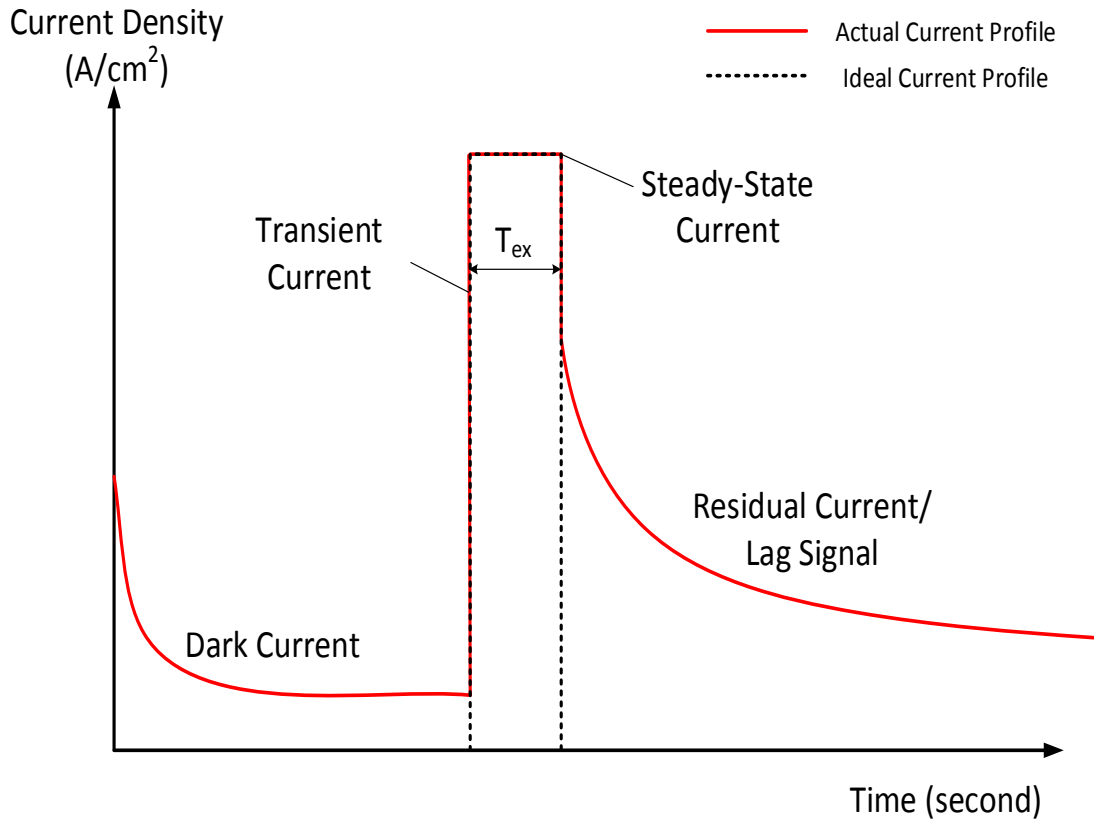
Figure 2.10: The current profile of a digital imaging detector exposed to a pulse of visible light. The profile shows the exponentially decaying dark current before the irradiation, the current peak due to the optical pulse excitation and the post-transit current after turning off the exposure [6]

## 2.7 Image Lag Artifacts

Image lag and ghosting are two common artifacts encountered in digital detectors. Although the terms are used interchangeably, lag and ghosting have very different definitions in technical terms. Ghosting is defined as the change in sensitivity of the X-ray imaging detectors due to previous radiation exposure. Ghosting reduces the pixel sensitivity of the detector thereby producing lower quality image in the subsequent exposures. In

33

image lag, some of the image charges from a previous exposure are carried onto the subsequent images. Image lag occurs due to the inherent structural defects in the photoconductor such as defect states in the mobility gap.

Compared to Computed radiography (CR) detectors, digital detectors such as FPDs have a much shorter time interval between exposures. Therefore, when a readout voltage is applied across the active matrix array, not all photogenerated carriers are collected for image processing. The carriers captured in deep traps can remain immobile for several minutes to hours. The trapped carriers are eventually released after readout to form a residual current. The lag signal from previous exposures interferes with subsequent images to produce artifacts such as image lag. For example, the image in Figure 2.11 below shows a case of image lag artifact during medical diagnosis. The portion inside the white bracket is the residual image of lead markers from the previous exposure. The lead markers represent the technologist's initial. They have sharp contrast and are easy to interpret as an artifact. However, there are other objects that appear in images due to image lag but are much harder to distinguish or might even mimic certain clinical findings. This can lead to severe consequences in medical diagnosis and treatment.
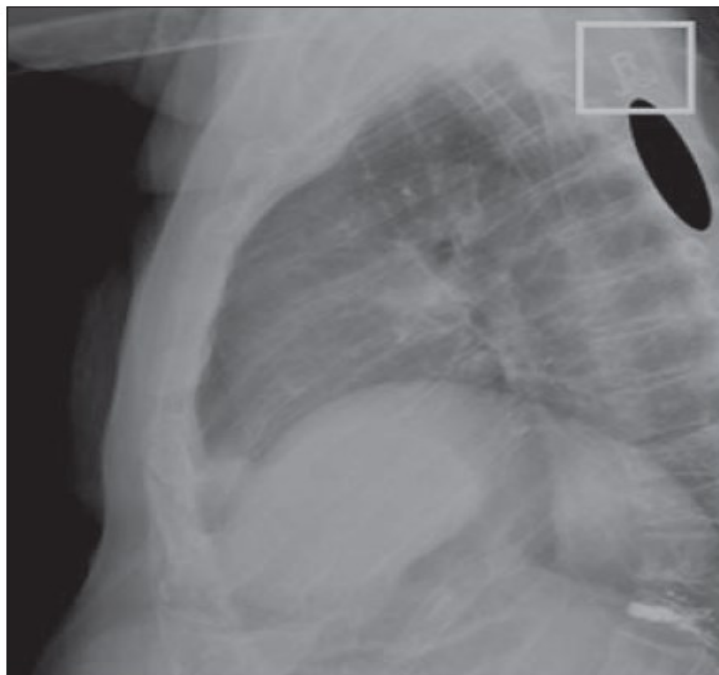
Figure 2.11: An example of image artifacts due to image lag during a medical examination [8].

## 2.8 Summary

Some important topics related to this thesis have been reviewed in this chapter. The widely used digital detectors known as flat-panel detectors have been introduced. The operating mechanism of the two types of flat-panels detectors, direct and indirect detectors, has been discussed. The charge read-out technique in FPDs using the active-matrix array has been explained as well. Since, amorphous selenium is a common photoconductor and has been used for this thesis, the structural and carrier transport properties of a-Se has been discussed. The localized density-of-states distribution in a-Se based on the Abkowitz has been presented. The defects and traps present in the mobility gap repeatedly captures and

35

releases carriers and often results in image artifacts such as image lag. The different carrier release mechanisms from the traps were also explained. Finally, image lag and its effect in medical diagnosis have been briefly discussed.

# CHAPTER 3: PROPOSED MATHEMATICAL MODEL FOR PHOTOCURRENT AND LAG SIGNAL ANALYSIS

## 3.1 Introduction

The excellent photoconductive properties of amorphous selenium have been well-known for more than three decades. a-Se is a top choice as photoconductor in imaging detectors commonly used for medical applications. When an a-Se based detector is exposed to electromagnetic excitation, be it X-rays or visible light, a photocurrent immediately starts to increase in magnitude (transient current) and then maintains a constant value for the remaining duration of exposure (steady-state current). Ideally, the photocurrent should return to zero as soon as the exposure is removed. However, in reality, an exponentially decaying current flows in the detector even after removal of the exposure. This is known as the lag signal. It is an undesirable phenomenon as it results in image lag artifacts which can lead to erroneous medical diagnosis.

In this thesis, a mathematical model for transient photocurrent and lag signal in imaging detectors for both X-ray and visible light exposure has been developed by considering charge carrier trapping and detrapping in the energy distributed defect states under exponentially distributed carrier generation across the photoconductor. The X-ray energy range used for most medical applications is in keV and the X-ray attenuation profile is exponentially decaying. Hence, in the model, an exponentially decaying carrier generation rate was considered since the rate of generation follows the X-ray absorption profile across

the photoconductor thickness. The model for the transient and steady-state carrier distributions and hence the photocurrent has been developed by solving the carrier continuity equation for both holes and electrons. The residual (commonly known as lag signal) current is modeled by solving the trapping rate equations considering the thermal release and trap filling effects.

The detector structure consists of a bulk photoconductor, such as a-Se in this case, of thickness $L$ that is sandwiched between two parallel plate electrodes. The lateral dimensions of the detector are much greater than its thickness $L$. The radiation-receiving electrode (top electrode) can be either positively or negatively biased with a voltage $V$ to establish an electric field $F$ in the photoconductor. In this model, the bias is assumed to be positive. Hence, the electrons drift towards the radiation-receiving electrode and the holes travel in the opposite direction to the back electrode where they are collected by the active matrix array. The direction of the hole and electron drift is interchanged if a negative bias is applied. The detector may be exposed to X-rays or optical excitation depending on the application. The charge carrier concentrations under normal dose in diagnostic medical imaging (e.g., mammography or chest radiography) and real-time imaging (e.g., fluoroscopy) are not high enough to perturb the electric distribution [50] (see Appendix A). Therefore, the electric field remains relatively uniform across the photoconductor layer (i.e., small signal analysis is a valid assumption). Since the mean energy and penetration depth of X-rays is much higher than light, the photoconductor thickness for X-ray exposure can vary between 200 to 1000 μm depending on the application but for optical irradiation, the photoconductor thickness is about 15 μm. The following assumptions were made while developing the model:

(i) The applied electric field remains uniform across the photoconductor.

(ii) Due to the high electric field applied across the photoconductor, the diffusion current is negligible compared to the drift current.

(iii) The thermally generated carrier concentration in the detector is negligible as compared to photo carriers.

(iv) The loss of carriers by deep trapping is more significant than bimolecular recombination.

(v) The initial trapped carrier concentration is zero.

## 3.2 Model for X-ray Excitation

X-rays are short wavelength and highly energetic electromagnetic radiation. They have a low attenuation coefficient, thus penetrating deep within the photoconductor. As shown in Figure 3.1, the X-ray photon intensity along the photoconductor decreases exponentially as $N(x) = N_0 \exp(-\alpha x)$, where $N_0$ is the photon intensity at $x = 0$ and $\alpha$ is the linear attenuation coefficient. Therefore, the EHP generation rate also follows an exponential pattern given by $G(x) = G_0 \exp(-\alpha x)$, where $G_0$ is the carrier generation rate at $x = 0$.
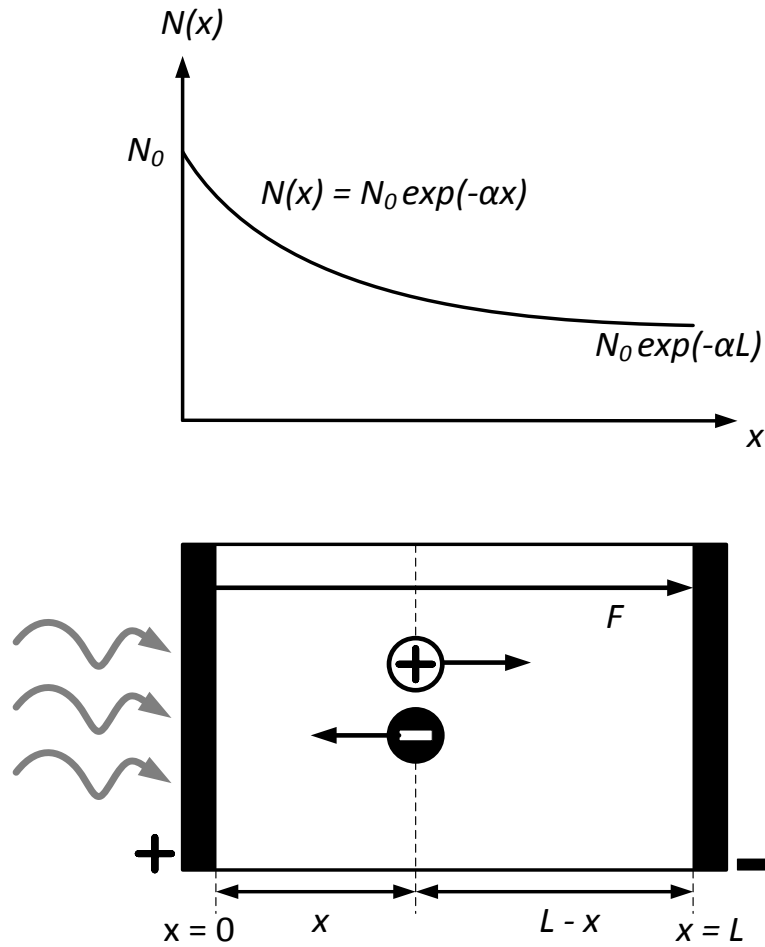
Figure 3.1: Exponentially decaying photon intensity along the photoconductor length $L$ (top).The electron-hole pair generation in the bulk of the photoconductor due to X-ray exposure. The carriers drift in opposite directions due to the electric field $F$ (bottom).

Unlike optical excitation, X-rays generate electron-hole pairs throughout the bulk of the photoconductor. Due to the applied electric field, the carriers overcome their Coulombic attraction and drift in opposite directions along the field lines. If the EHP generation occurs at a distance $x$ from the top electrode, the electron has to travel a distance $x$ and the hole has to travel ($L$-$x$) to reach their respective electrodes. As a result, the hole concentration

increases whereas the concentration of electrons decreases along the photoconductor length *L*.

## 3.2.1 Carrier Concentration Profile

The carrier generation-recombination process in the a-Se detector can be described by the space and time dependent continuity equation shown below:

$$\frac{\partial p(x,t)}{\partial t} + \mu_h p \frac{\partial F}{\partial x} + \mu_h F \frac{\partial p(x,t)}{\partial x} + D_p \frac{\partial^2 p(x,t)}{\partial x^2} = G - R \tag{3.1}$$

Since a uniform electric field *F* was applied across the photoconductor, the diffusion current is negligible compared to the drift current. Therefore, the spatially varying electric field and diffusion current terms in equation (3.1) are ignored to give us the following equation.

$$\frac{\partial p}{\partial t} + \mu_h F \frac{\partial p}{\partial x} = G_0 \exp(-\alpha x) - \frac{p}{\tau_h} \tag{3.2}$$

where *p* is the space and time dependent free hole concentration, *x* is the distance in the photoconductor layer from the radiation-receiving electrode, *t* is the time, $\mu_h$ is the effective hole drift mobility, $\tau_h$ is the hole lifetime, $G_0$ is the electron-hole pair (EHP) generation rate at *x* = 0, $\alpha$ is the linear attenuation coefficient, *F* (=*V/L*) is the applied electric field and *L* is the photoconductor thickness.

The photogenerated holes drift towards the bottom electrode and electrons move towards the radiation-receiving top electrode due to the positive applied bias. Obviously, the initial condition for holes is zero, i.e., $p(x,0) = 0$. On the other hand, as the holes drift to the back electrode immediately after generation, there will not be any holes present at the infinitesimal distance at $x = 0$ which implies that the boundary condition is $p(0,t) = 0$ [14].

Solving the continuity equation in (3.2) using the initial and boundary conditions for holes gives

$$p(x,t) = \begin{cases} A\exp(-\alpha x)\{1 - \exp(-t/\tau_h + \alpha\mu_h Ft)\}; x > \mu_h Ft \\ \\ A[\exp(-\alpha x) - \exp(-x/\mu_h\tau_h F)]; x < \mu_h Ft \end{cases} \tag{3.3}$$

where $A = \dfrac{G_0\tau_h}{1 - \alpha\mu_h\tau_h F}$

As mentioned earlier, immediately after exposure, the current almost instantaneously increases in magnitude (transient current) and then maintains a constant value for the remaining duration of exposure (steady-state). In equation (3.3), the expressions for $x > \mu_h Ft$ and $x < \mu_h Ft$ represent the free hole concentration during the transient and steady-state periods, respectively. The expression of $G_0$ (in $cm^{-3} s^{-1}$) is given by

$$G_0 = \frac{\phi_0 E_{ph}\alpha}{T_{ex}W_\pm}(cm^{-3}s^{-1}) \tag{3.4}$$

where $E_{ph}$ is the X-ray photon energy in eV, $W_\pm$ is the EHP creation energy in eV, $\alpha$ is the attenuation coefficient in cm$^{-1}$ and $T_{ex}$ is the exposure time in seconds. The incident photon fluence which is defined as the number of photons received by a surface per unit area is given by the formula [51]

$$\phi_0 = \frac{5.45 \times 10^{13} X}{(\alpha_{air}/\rho_{air})E_{ph}}(photons/cm^3)$$

(3.5)

where $X$ is the X-ray exposure in roentgens, $\alpha_{air}$ and $\rho_{air}$ are the energy absorption coefficient and the density of air respectively ($\alpha_{air}/\rho_{air}$ is in cm$^2$ g$^{-1}$) [51].

Now, the electron continuity equation is given by

$$\frac{\partial n}{\partial t} - \mu_e F \frac{\partial n}{\partial x} = G_0 \exp(-\alpha x) - \frac{n}{\tau_e}$$

(3.6)

where $n$ is the space and time dependent free electron concentration, $\mu_e$ is the effective electron drift mobility and $\tau_e$ is the electron lifetime.

Using a similar line of argument that we used for holes, the initial and boundary conditions for free electrons are $n(x,0) = 0$ and $n(L,t) = 0$ respectively. Solving the electron continuity equation using the above initial and boundary conditions, the expression for free electron concentration was found to be

$$n(x,t) = \begin{cases} B\exp(-\alpha x)\left\{1 - \exp\left(\dfrac{-t}{\tau_e} - \alpha\mu_e Ft\right)\right\}; L - x > \mu_e Ft \\[4mm] B\left\{\exp(-\alpha x) - \exp(-\alpha L)\exp\left(-\dfrac{(L-x)}{\mu_e \tau_e F}\right)\right\}; L - x < \mu_e Ft \end{cases} \quad (3.7)$$

where $B = \dfrac{G_0 \tau_e}{1 + \alpha\mu_e \tau_e F}$

## 3.2.2 Transient and Steady-State Current

The Shockley – Ramo Theorem allows us to easily calculate the instantaneous electric current induced by a charge moving in the vicinity of an electrode. Based on the theorem, the photocurrent density due to hole drift can be given by equation (3.8) [7]

$$J_h(t) = \frac{e\mu_h F}{L} \int_0^L p(x,t)\,dx \quad (3.8)$$

The photocurrent steadily increases in magnitude after exposure. The hole current reaches the maximum value at the the hole transit time, $T_h = L/\mu_h F$. From the transit time up to the duration of exposure, the current maintains a constant value. Inserting equation (3.3) into equation (3.8) and simplifying the integration gives the hole current density, $J_h$, which is

$$J_h(t) = \begin{cases} \dfrac{Ae\mu_h F}{\alpha L}\left\{\left[1 - \exp\left(-t/\tau_h\right)\right](1 - \alpha\mu_h \tau_h F) - \exp(-\alpha L)\left[1 - \exp\left(-t/\tau_h + \alpha\mu_h Ft\right)\right]\right\}; 0 < t < T_h \\[4mm] \dfrac{Ae\mu_h F}{\alpha L}\left\{1 - \alpha\mu_h \tau_h F + \alpha\mu_h \tau_h F\exp\left(\dfrac{-T_h}{\tau_h}\right) - \exp(-\alpha\mu_h FT_h)\right\}; t > T_h \end{cases} \quad (3.9)$$

44

The corresponding Ramo-Shockley theorem based electron current expression is given by

$$J_e(t) = \frac{e\mu_e F}{L} \int_0^L n(x,t)dx \tag{3.10}$$

Inserting equation (3.7) into equation (3.10) results in equation (3.11) below

$$J_e(t) = \begin{cases} \dfrac{Be\mu_e F}{\alpha L}\left\{\left[1-\exp\left(-t/\tau_e - \alpha\mu_e Ft\right)\right]-\exp(-\alpha L)\left[1-\exp\left(-t/\tau_e\right)\right](1+\alpha\mu_e\tau_e F)\right\};0<t<T_e \\[4mm] \dfrac{Be\mu_e F}{\alpha L}\left\{[1-\exp(-\alpha L)]-\alpha\mu_e\tau_e F\exp(-\alpha L)\left[1-\exp\left(-L/\mu\tau_e F\right)\right]\right\};t>T_e \end{cases} \tag{3.11}$$

The total photocurrent density is sum of the hole and electron current components.

$$J_p = J_h + J_e \tag{3.12}$$

## 3.2.3 Photocurrent decay after X-ray excitation

The photocurrent continues to flow up to the carrier transit time after turning off the irradiation. Let us say that $t'$ is the time interval after the X-ray excitation is turned off at $T_{ex}$. From time $T_{ex}$ when the exposure is removed, the generation rate $G_0 = 0$. Therefore, the hole continuity equation is given by

$$\frac{\partial p'}{\partial t'} + \mu_h F\frac{\partial p'}{\partial x} = -\frac{p'}{\tau_h} \tag{3.13}$$

where $p'(x, t')$ is the new free carrier concentration.

45

Since the free carrier concentration at the end of exposure $p(x, T_{ex})$ will be the initial carrier concentration after the exposure is removed, the initial condition is given by $p'(x,0) = p(x, T_{ex})$. The boundary condition, on the other hand, is $p'(0,t') = 0$. Inserting the new conditions into equation (3.13), we obtain

$$p'(x,t') = p(x - \mu_h F t', T_{ex}) \exp\left(-t'/\tau_h\right); \mu_h F t' < x < L \qquad (3.14)$$

The term $\exp\left(-t'/\tau_h\right)$ in equation (3.14) represents the reduction of the holes due to trapping whereas the term $p(x - \mu_h F t', T_{ex})$ represents the drift of the carriers along the photoconductor.

Using a similar line of argument for electrons and considering the initial conditions $n'(x,0) = n(x, T_{ex})$ and $n'(L,t') = 0$, we get the expression for the electron concentration after X-ray exposure in equation (3.15)

$$n'(x,t') = n(x + \mu_e F t', T_{ex}) \exp\left(-t'/\tau_e\right); 0 < x < (L - \mu_e F t') \qquad (3.15)$$

where $t' = t - T_{ex}$, and $T_{ex}$ is the duration of the X-ray excitation.

Figure 3.2 shows the spatially distributed hole and electron concentration along the photoconductor after removal of excitation at time $t' = 0$ and $t' > 0$. For positive bias, the holes drift towards the back electrode and electrons drift towards the top electrode. At $t' > 0$, the holes drift a distance $\mu_h F t'$ and electrons move a distance $L - \mu_e F t'$.
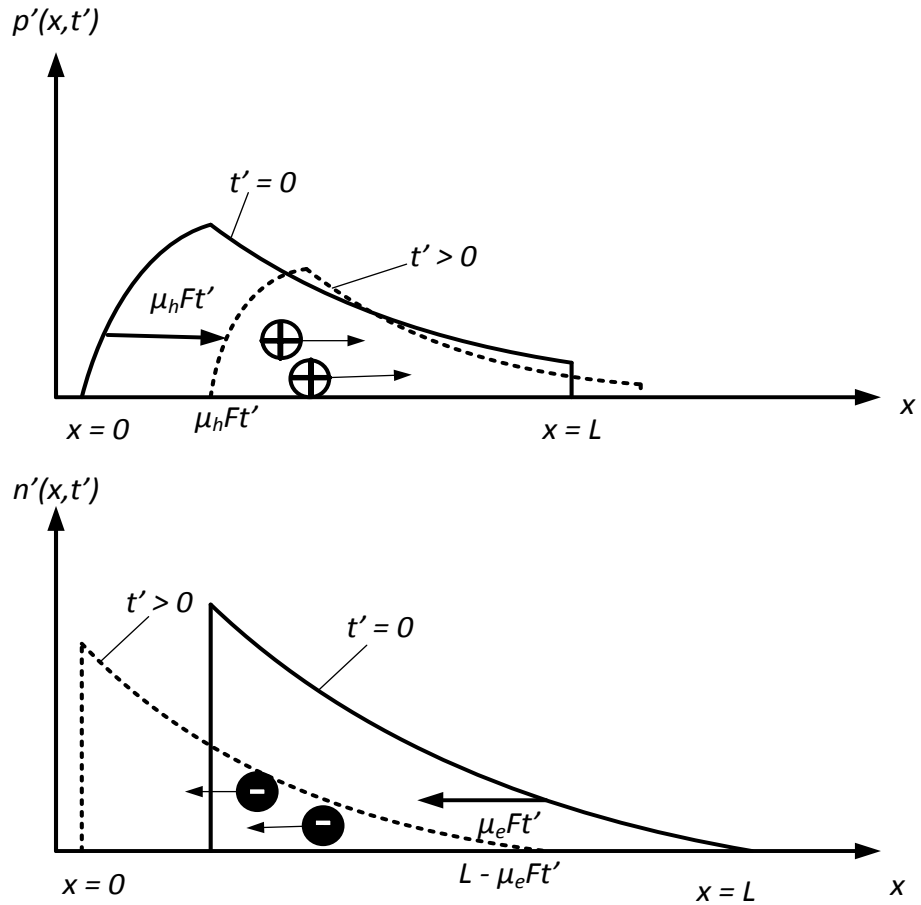
Figure 3.2: The drift of holes and electrons in a positively biased photoconductor after removal of exposure. At $t' > 0$, the holes drift a distance of $\mu_h F t'$ and electrons move a distance $L-\mu_e F t'$. $p'(x,t')$ represents the hole concentration profile and $n'(x,t')$ represents the electron concentration profile.

Since a positive bias is applied, at $t' > 0$, the holes drift a distance $\mu_h F t'$ and electrons move a distance $L-\mu_e F t'$. At any time $t'$, the holes must drift from $x = \mu F t'$ to $x = L$ to reach the back electrode. Therefore, the hole current density is given by

$$J_h(t') = \frac{e\mu_h F}{L} \int_{\mu_h Ft'}^{L} p'(x,t')dx \qquad (3.16)$$

On the other hand, electrons must travel from $x = L\text{-}\mu Ft'$ to $x = 0$ to reach the top electrode. The electron current density is given by

$$J_e(t') = \frac{e\mu_e F}{L} \int_{0}^{L-\mu_e Ft'} n'(x,t')dx \qquad (3.17)$$

For a long exposure, the carrier concentrations and photocurrent reach steady values before the end of the exposure. Inserting equation (3.14) into equation (3.16) and inserting equation (3.15) into equation (3.17) gives us equations (3.18) and (3.19) respectively.

$$J_h(t') = \frac{A e\mu_h Fe^{-t'/\tau_h}}{\alpha L} \left\{ 1 - e^{-\alpha(L-\mu_h Ft')} - \alpha\mu_h\tau_h F\left[1 - e^{-(L-\mu_h Ft')}\right] \right\}; t' \le T_h \qquad (3.18)$$

$$J_e(t') = \frac{B e\mu_e Fe^{-t'/\tau_e}}{\alpha L} \left\{ e^{-\alpha\mu_e Ft'} - e^{-\alpha L} - \alpha\mu_e\tau_e Fe^{-\alpha L}\left[1 - e^{-(L-\mu_e Ft')}\right] \right\}; t' \le T_e \qquad (3.19)$$

## 3.2.4 Residual Current or Lag Signal

As previously mentioned a transient decaying current is detected in a-Se flat-panel detectors a long time after the excitation is taken away. Carrier detrapping from the various (shallow as well as deep) trapping states, which appear as localized states or defects in the mobility gap in a-Se, is widely believed to be responsible for this residual current in a-Se

devices. The localized density of states, $N(E)$, in the lower and upper half of mobility gap in a-Se appear as exponential decays from the edges and two Gaussian curves in the middle. The outer Gaussian curve represents the shallow traps and lower one represents the deep traps [52]. The density of hole and electron trapping states in the midgap at a particular energy level $E$ from the valence and conduction band edges can be written, respectively, as [53]

$$N_h(E) = g_h \exp\left(-E/kT\right) + N_{h1} \exp\left\{\frac{-(E-E_{h1})^2}{\Delta E_{h1}{}^2}\right\} + N_{h2} \exp\left\{\frac{-(E-E_{h2})^2}{\Delta E_{h2}{}^2}\right\} \qquad (3.20)$$

$$N_e(E) = g_e \exp\left(-E/kT\right) + N_{e1} \exp\left\{\frac{-(E-E_{e1})^2}{\Delta E_{e1}{}^2}\right\} + N_{e2} \exp\left\{\frac{-(E-E_{e2})^2}{\Delta E_{e2}{}^2}\right\} \qquad (3.21)$$

where $T$ is the characteristics temperature, $g$ is the density of states at the band edge, $\Delta E$ is the standard deviation of the Gaussian curves, $N_1$ and $N_2$ are the peak values of the shallow traps at $E = E_1$ and deep traps at $E = E_2$, respectively. The subscript $h$ and $e$ stand for holes and electrons respectively.

The magnitude of the release current is directly proportional to the trapped carrier concentration, $p_t$, and inversely proportional to the carrier release time, $\tau_r$ . The residal current results due to the integrated contribution of the trapped carriers at the various energy states throughout the photoconductor.

The expression for the residual current density due to hole detrapping can be written as [54]

$$J_{rh}(t) = e\int_0^E\int_0^L \frac{p_t(x,T_{ex},E)}{\tau_{rh}(E)}\exp\left(-t/\tau_{rh}(E)\right)\left(1-x/L\right)dxdE \qquad (3.22)$$

where $p_t$ is the trapped hole concentration, $\tau_{rh}$ is the average hole release time and $T_{ex}$ is the exposure duration.

The rate of change of trapped carriers at a particular energy $E$ is equal to the net difference between the hole capture and release rates. Since the probability of a hole being captured is proportional to the number of empty defect states and the free hole concentration in the photoconductor, the kinetic rate equation for trapped holes at energy $E$ from the valence band edge is given by

$$\frac{\partial p_t(x,t,E)}{\partial t} = C_{th}N(E)\left\{1-\frac{p_t(x,t,E)}{N(E)}\right\}p(x,t)-\frac{p_t}{\tau_{rh}} = C_{th}N_h(E)p(x)-\frac{p_t}{\tau'_{rh}} \qquad (3.23)$$

where

$$\frac{1}{\tau'_{rh}} = C_{th}p(x)+\frac{1}{\tau_{rh}} \qquad (3.24)$$

Considering the principles of detailed balance, the capture coefficient for free holes, $C_{th} = v_0/g_h kT$, where, $v_0$ is the attempt-to-escape frequency, $T$ is the absolute temperature and $g_h kT$ is approximately the effective density of states at the valence band [55].

In the presence of an electric field, the release time from localized traps can be written as

$$\frac{1}{\tau_{rh}} = \nu_0 \exp\left[-\left(\frac{E - \phi(F)}{kT}\right)\right] \qquad (3.25)$$

The electric field lowers the potential barrier for a trapped carrier making it easier for the carrier to escape. $\phi(F)$ is the field-dependent barrier lowering potential for trapped carriers. For the thermally-assisted tunneling mechanism, $\phi(F) = aF$ where $a$ is the effective tunneling distance along the field. On the other hand, $\phi(F) = \sqrt{eF/\pi \varepsilon_s}$ for one-dimensional Poole-Frenkel mechanism where $\varepsilon_s = \varepsilon_0 \varepsilon_r$ is the permittivity of a-Se [56].

The solution of first-order differential equation in (3.23) gives us

$$p_t(x, t, E) = C_{th} N_h(E) p(x) \tau'_{rh} \left\{ 1 - \exp\left(-\frac{t}{\tau'_{rh}}\right) \right\} \qquad (3.26)$$

Hence, at the end of exposure, i.e., at $t = T_{ex}$, equation (3.26) becomes

$$p_t(T_{ex}, x, E) = C_t N_h(E) p(x) \tau'_{rh} \left(1 - \exp\left(\frac{-T_{ex}}{\tau'_{rh}}\right)\right) \qquad (3.27)$$

Inserting equation (3.27) into equation (3.22) gives

$$J_{rh} = e \int_0^E \frac{C_t N_h(E)}{\tau_{rh}(E)} \exp\left(-\frac{t}{\tau_{rh}(E)}\right) \left\{ \int_0^L p(x) \tau'_{rh} \left[ 1 - \exp\left(\frac{-T_{ex}}{\tau''_{rh}}\right) \right] \left(1 - \frac{x}{L}\right) dx \right\} dE \qquad (3.28)$$

Similarly, the residual current density due to electron detrapping is

$$J_{re} = e \int_0^E \frac{C_{te} N_e(E)}{\tau_{re}(E)} \exp\left(-t/\tau_{re}(E)\right) \left\{ \int_0^L n(x)\tau'_{re} \left[1 - \exp\left(-T_{ex}/\tau'_{re}\right)\right] \left(x/L\right) dx \right\} dE \qquad (3.29)$$

where $\dfrac{1}{\tau'_{re}} = C_{te} n(x) + \dfrac{1}{\tau_{re}}$ and $C_{te} = \dfrac{v_0}{g_e kT}$ $\qquad\qquad$ (3.30)

The total residual current density is given by

$$J_r = J_{rh} + J_{re} \qquad\qquad\qquad (3.31)$$

## 3.3 Model for Optical Excitation

When visible light is exposed to a detector, most of it is absorbed near the surface of the detector due to the very high attenuation coefficient of light. As a result, the photogeneration in the photoconductor occurs very close to the radiation receiving electrode. The electrons are immediately lost as they recombine in the radiation-receiving electrode which is positively biased and the holes drift across the amorphous selenium towards the back electrode. Hence, for optical irradiation, only hole contribute to the resulting photo and residual current and the effect of electrons can be neglected. Moreover, the photoconductor length can be a small as 15 μm as the most of the radiation is absorbed close to the surface. The EHP generation and carrier transport in an optically excited imaging detector is shown in Figure 3.3 below.
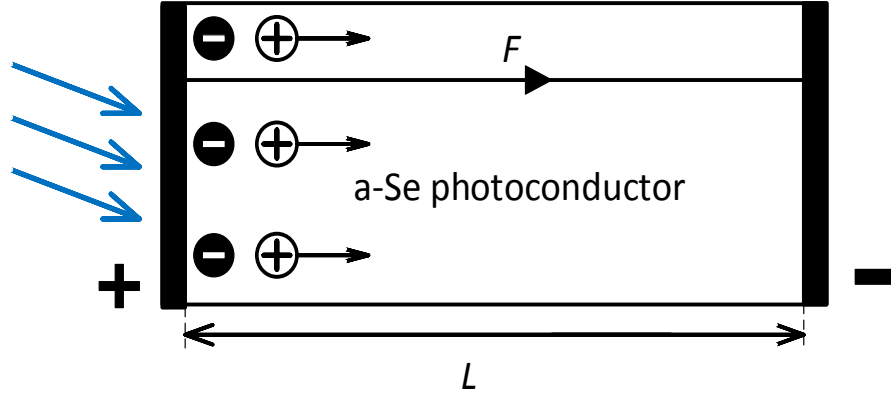
Figure 3.3: Electron-hole pair generation in an optically illuminated imaging detector. Since, light has high attenuation coefficient, the photogeneration occurs close to the surface of the photoconductor. The electrons are immediately lost in the top electrode and the holes drift across the photoconductor to reach the back electrode.

## 3.3.1 Carrier Concentration and Photocurrent

It was shown for the X-ray model how the continuity equation can be solved using appropriate limits to obtain the free carrier concentration in the detector. Using the same procedure, the free hole concentration for optical irradiation is given by

$$p(x,t) = \begin{cases} A\exp(-\alpha x)\{1-\exp(-t/\tau_h+\alpha\mu_h Ft)\}; x > \mu_h Ft \\ \\ A[\exp(-\alpha x)-\exp(-x/\mu_h\tau_h F)]; x < \mu_h Ft \end{cases} \qquad (3.32)$$

where $A = \dfrac{G_0\tau_h}{1-\alpha\mu_h\tau_h F}$

In this case, the expression of $G_0$ (in $cm^{-3}\,s^{-1}$) is given by

53

$$G_0 = \eta_q \frac{I_0 \alpha}{E_{ph}} \tag{3.33}$$

where $E_{ph}$ is the light photon energy, $I_0$ is the intensity of light and $\eta_q$ is the quantum yield. Using a similar line of argument that we used for holes, the initial and boundary conditions for free electrons are $n(x,0) = 0$ and $n(L, t) = 0$ respectively. Solving the electron continuity equation using the above initial and boundary conditions, the expression of electron concentration and photocurrent are

$$n(x,t) = \begin{cases} B\exp(-\alpha x)\left\{1 - \exp\left(\dfrac{-t}{\tau_e} - \alpha\mu_e Ft\right)\right\}; L - x > \mu_e Ft \\[4mm] B\left\{\exp(-\alpha x) - \exp(-\alpha L)\exp\left(-(L-x)\Big/\mu_e \tau_e F\right)\right\}; L - x < \mu_e Ft \end{cases} \tag{3.34}$$

where $B = \dfrac{G_0 \tau_e}{1 + \alpha\mu_e \tau_e F}$ .

Under optical excitation, the linear absorption coefficient is very high. The a-Se layer thickness is 15 μm, irradiation wavelength is 468 nm and $\alpha = 1.55 \times 10^5$ cm$^{-1}$. The electron concentration deceases very rapidly with distance and becomes practically zero in most of the thickness (as seen in Figure 4.15 in Chapter 4). Therefore, the electron concentration is negligible as compared to the hole concentration. In the limit of extremely high absorption coefficient, $n(x) \approx 0$ and steady-state hole concentration,

$$p(x) = \frac{\eta_q I_0}{\mu_h FE_{ph}} \exp\left(- x / \mu_h \tau_h F\right)$$

(3.35)

The photocurrent density due to hole drift [9] is given by

$$J_h = \frac{e\mu_h F}{L} \int_0^L p(x,t)dx = \frac{eI_0 \eta_q}{E_{ph}} \left(\frac{\mu_h \tau_h F}{L}\right)\left[1 - \exp\left(\frac{L}{\mu_h \tau_h F}\right)\right]$$

(3.36)

## 3.3.2 Residual Current

The rate of change of trapped holes at a certain energy level $E$ is given by the net difference between the number of holes trapped and the numbers of holes released from traps at $E$ as shown below.

$$\frac{\partial p_t(E)}{\partial t} = C_t N(E)\left\{1 - \frac{p_t(E)}{N(E)}\right\}p(x) - \frac{p_t}{\tau_r}$$

(3.37)

where $p_t$ is the concentration of trapped holes, $C_t$ is the hole capture coefficient. Considering the principles of detailed balance, $C_t = \frac{v_0}{g_h kT}$ where, $v_0$ is the attempt-to-escape frequency, $g_h$ is the density of states at the valence band edge and $g_h kT$ is approximately the effective density of states at the valence band. $\tau_r$ is known as the carrier release time given by

$$\tau_r = \frac{1}{v_o} \exp\left\{\frac{[E - e\phi(F)]}{kT}\right\}$$

(3.38)

55

Moreover, $N_h(E)$ is the density of states of holes at the energy level $E$ given by

$$N_h(E) = g_h \exp\left(-E/kT\right) + N_{h1} \exp\left\{\frac{-(E - E_{h1})^2}{\Delta E_{h1}{}^2}\right\} + N_{h2} \exp\left\{\frac{-(E - E_{h2})^2}{\Delta E_{h2}{}^2}\right\} \tag{3.39}$$

$T$ is the characteristic temperature, $N_{h1}$ and $N_{h2}$ are the peak values of the shallow traps at $E=E_{h1}$ and deep traps at $E=E_{h2}$ respectively. Rearranging equation (3.37) will result in

$$\Rightarrow \frac{\partial p_t(E)}{\partial t} = C_t N(E) p(x) - \left[C_t p(x) + \frac{1}{\tau_r}\right] p_t = C_t N(E) p(x) - p_t/\tau' \tag{3.40}$$

where $1/\tau' = C_t p(x) + 1/\tau_r$

$$\Rightarrow \frac{\partial p_t}{\partial t} + \frac{p_t}{\tau'} = C_t N(E) p(x) \tag{3.41}$$

where $p$ is the steady-state free hole concentration.

Solving equation (3.41) gives us the trapped hole concentration shown below.

$$\therefore p_t(t) = C_t N(E) p(x) \tau' \left\{1 - \exp\left(-t/\tau'\right)\right\} \tag{3.42}$$

For the time $t = T_{ex}$,

$$p_t(T_{ex}, x, E) = C_t N(E) p(x) \tau' \left\{1 - \exp\left(-T_{ex}/\tau'\right)\right\} \tag{3.43}$$

The hole release current is given by

$$J_{rh} = e \int_0^E \int_0^L \frac{p_t(T_{ex,}x,E)}{\tau_r(E)} \left\{ \exp\left(-t/\tau_r(E)\right) \right\} \left(1 - x/L\right) dx dE \qquad (3.44)$$

Since the photoconductor thickness is very small (ie. 15 μm), the exponential term in equation (3.35) goes to 1, ie. $\exp(-x/\mu_h\tau_h F) \approx 1$. This implies that the free hole concentration can be considered spatially uniform.

$$p(x) = p = \frac{n_q I_0}{\mu_h F E_{ph}} \qquad (3.45)$$

If $p(x)$ is uniform, it follows from equation (3.42) that $p_t$ is also spatially non-varying. Hence, ignoring spatial variation in $p_t,$ the release current for optical irradiation is

$$\Rightarrow J_{rh} = \frac{eL}{2} \int_0^E \frac{p_t(T_{ex},x,E)}{\tau_r(E)} \exp\left(-t/\tau_r(E)\right) dE \qquad (3.46)$$

## 3.4 Summary

In this chapter, a physics based mathematical model has been proposed for the current profile in flat-panel detectors for exponential carrier generation. The model has been developed by considering the continuous trapping and detrapping of charge carriers in the energy distributed defects states in the mobility gap of amorphous semiconductors. Firstly, a model for X-ray excitation has been developed by solving the space and time dependent continuity equation. The free carrier concentration and photocurrent was obtained.

Expressions for the transient photocurrent and the photocurrent decay after removal of excitation has also been obtained. The trapping rate equation has been used to obtain the trapped carrier concentration and residual current. Next, a model for visible light excitation has been developed. Since light is highly attenuated in the photoconductor, certain valid simplifications have been applied to this model. The expressions for carrier concentration, photocurrent and residual current for optical excitation have been derived as well.

# CHAPTER 4: RESULTS AND DISCUSSION

## 4.1 Introduction

In the previous chapter, it was shown how a mathematical model for a-Se detectors has been developed using continuity equation and the Ramo-Shockley theorem for X-rays and visible light exposure. Due to the high attenuation coefficient of visible light, it was possible to simplify the model by making certain assumptions such as negligible electron contribution to the photocurrent.

The equations developed in Chapter 3 were used to plot graphs of carrier concentration, photo and residual current using the software MATLAB. The effects of radiation intensity, ambient temperature, electric field, etc. on the current were quantitatively analyzed. Moreover, the models were verified by fitting the theoretical results with published experimental data.

## 4.2 Results for X-ray Excitation

### 4.2.1 Carrier Concentration

The carrier concentration, photo and residual current for X-ray exposure were studied for two particular cases of medical imaging applications namely chest radiography and mammography. The mean photon energy for chest radiography and mammography are taken as 60 keV and 20 keV respectively. The photoconductor thickness, $L$, is taken as 1000

μm for chest radiography and 200 μm for mammography. The exposure time, $T_{ex}$, is assumed to be 10 ms. The effective carrier mobilities, $\mu_h = 0.12$ and $\mu_e = 0.003$ cm$^2$/V-s are taken in all calculations. The exposure range for chest radiography varies from 30 μR to 3000 μR with the mean exposure being 300 μR whereas it varies from 0.6 mR to 240 mR with the mean exposure being 12 mR in mammography.

Figure 4.1 shows the transient and steady-state hole concentration profiles across the photoconductor thickness for chest radiography at various times ($t = 0.25$ $T_h$, 0.5 $T_h$ and $T_h$) and an applied electric field of $F = 10$ V/μm at room temperature (22 °C). The nominal exposure of $X = 300$ μR for chest radiography is used. The hole concentration profiles are shown for two hole lifetimes, $\tau_h = 50$ and 5 μs, since it normally varies within this range. The EHP creation energy $W_\pm$ is 45 eV for $F = 10$ V/μm and $E_{ph} = 60$ keV [36]. The hole concentration increases with time and reaches a steady value at $t = T_h$. The hole concentration at $t = 0.25T_h$ and $t = 0.50T_h$ represents the transient hole concentration. They initially increase in magnitude but starts to decrease exponentially at $0.25L$ and $0.50L$ along the photoconductor respectively. Obviously, the hole concentration is higher for higher carrier lifetime. However, the difference in the magnitude at the two carrier lifetimes is more significant for steady-state hole concentration than for transient concentration. The steady-state current densities for hole transport are $6.6630 \times 10^{-8}$ and $4.1897 \times 10^{-8}$ A/cm$^2$ for $\tau_h = 50$ and 5 μs, respectively.
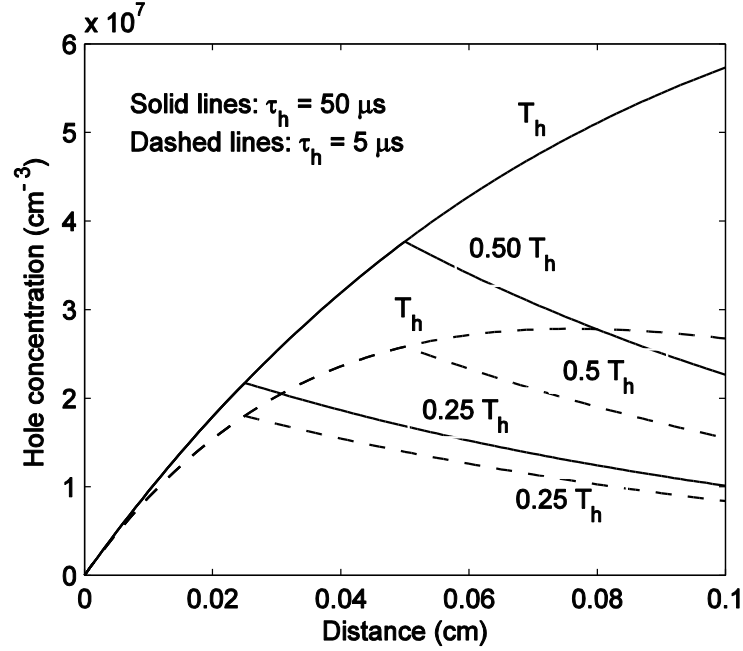
Figure 4.1: Hole concentration versus distance from the radiation-receiving electrode in a-Se chest radiographic detectors at room temperature and an applied electric field of 10 V/μm. The hole concentration is plotted at various times ($t = 0.25\ T_h$, $0.5\ T_h$ and $T_h$) for two hole lifetimes. The solid lines represent the hole concentration at $\tau_h = 50$ μs and the dashed lines represent the hole concentration at $\tau_h = 5$ μs [57].

Figure 4.2 shows the transient and steady-state electron concentration profiles across the photoconductor thickness for chest radiography at various times ($t = 0.25\ T_e$, $0.5\ T_e$ and $T_e$) and an applied electric field of $F = 10$ V/μm at room temperature. The electron concentration profiles are shown for two electron lifetimes, $\tau_e = 500$ and 50 μs, to observe the effect of carrier transport properties on electron concentration. The steady-state current densities for the electron transport are $4.1687 \times 10^{-8}$ and $1.4406 \times 10^{-8}$ A/cm$^2$ for $\tau_e = 500$ and 50 μs, respectively. As evident from Figures 4.1 & 4.2, the magnitude of electron concentration is much higher than that of hole concentration because of higher lifetime and

61

lower transit time of electrons. However, the steady-state photocurrent density due to the hole transport is higher than that due to the electron transport as the hole mobility is much greater (approximately 40 times).
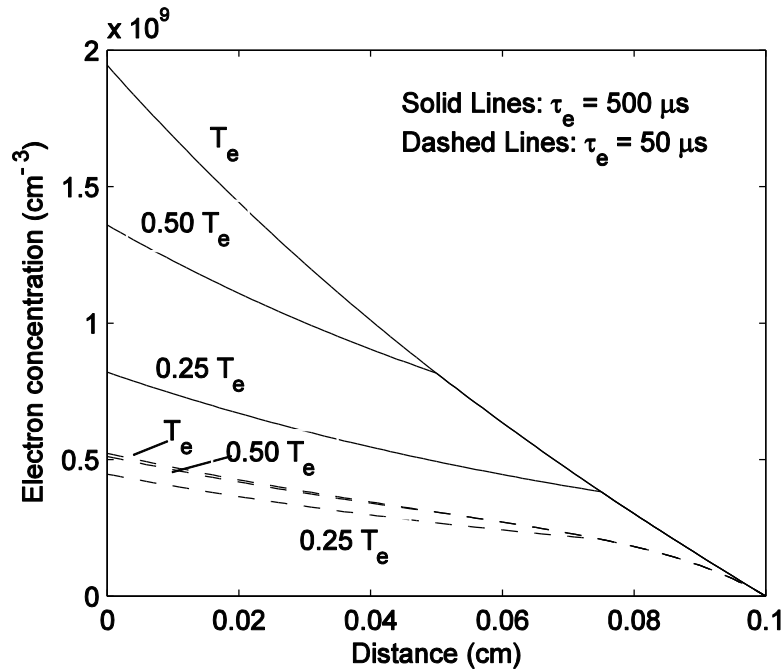


Figure 4.2: Electron concentration versus distance from the radiation-receiving electrode in a-Se chest radiographic detectors at room temperature and an applied electric field of 10 V/μm. The electron concentration is plotted at various times ($t = 0.25\ T_e$, $0.5\ T_e$ and $T_e$) for two electron lifetimes. The solid lines represent the electron concentration at $\tau_e = 500$ μs and the dashed lines represent the electron concentration at $\tau_e = 50$ μs [57].

The hole and electron concentration profiles for mammographic applications are shown in Figures 4.3 and 4.4. The nominal exposure of $X = 12$ mR for mammography is applied. The EHP creation energy $W_\pm$ is about 60 eV for $F = 10$ V/μm and $E_{ph} = 20$ keV [36]. The steady-state current densities for hole and electron transports are $3.24 \times 10^{-7}$ and $9.29 \times 10^{-8}$

A/cm$^2$ , respectively. When compared to chest radiography, it can be observed that the steady-state hole concentration for mammography is about 4 times higher for the same hole lifetime of 50 µs and the steady-state electron concentration is about 5 times higher for electron lifetime of 500 µs.
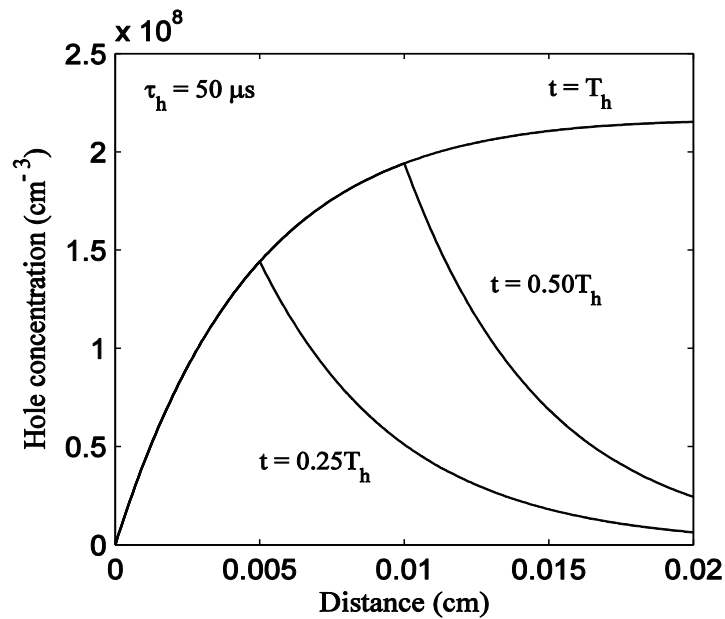


Figure 4.3: Hole concentration versus distance from the radiation-receiving electrode in a-Se mammographic detectors at room temperature and an applied electric field of 10 V/µm. The hole concentration are plotted at various times ($t$ = 0.25 $T_h$, 0.5 $T_h$ and $T_h$) for the hole lifetime $\tau_h$ = 50 µs [57].
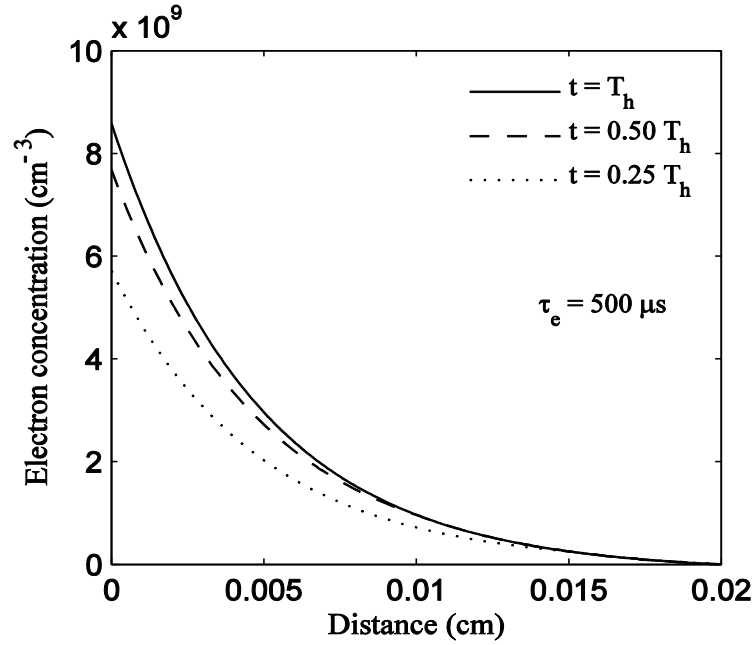
Figure 4.4: Electron concentration versus distance from the radiation-receiving electrode in a-Se mammographic detectors at room temperature and an applied electric field of 10 V/μm. The electron concentration are plotted at various times ($t$ = 0.25 $T_e$, 0.5 $T_e$ and $T_e$) for the electron lifetime $\tau_h$ = 500 μs [57].

## 4.2.2 Transient Photocurrent

Next, the variation of the transient photocurrent with time for mammography and chest radiography and the contribution of the electron and hole current to the total photocurrent is analysed. Figure 4.5 shows the transient photocurrent as a function of time for mammographic a-Se detectors at an applied electric field of $F$ = 10 V/μm. The nominal exposure of $X$ = 12 mR for mammography is applied. The hole and electron currents increases with time and reach the steady values at $t = T_h$ and $T_e$ respectively. The magnitude

of the steady state hole current is much higher than the electron current. Moreover, the hole current approaches steady-state much faster than electron current due to shorter hole transit time. Thus the shape of the total photocurrent initially has a very fast rising and then a slowly rising patterns.
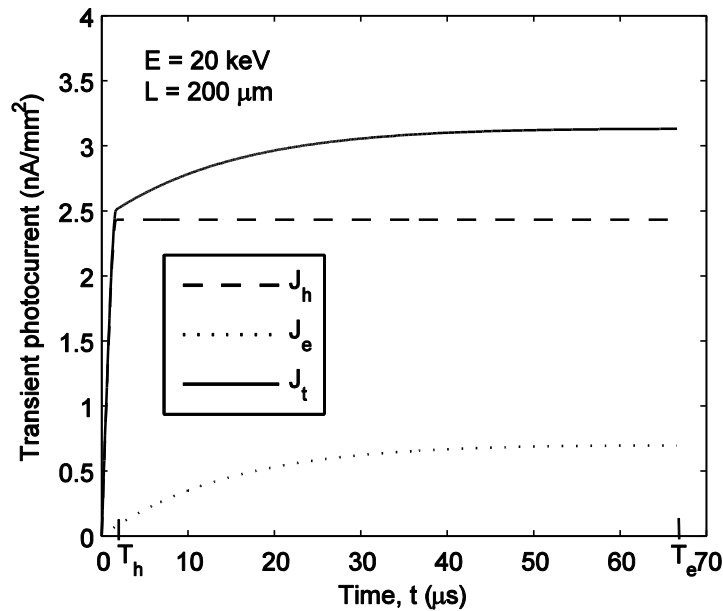


Figure 4.5: Transient photocurrent versus time in a-Se mammographic detectors at room temperature and electric field of 10 V/μm. The dotted, dashed and solid lines represent the electron, hole and total current respectively [58].

Figure 4.6 shows the transient photocurrent as a function of time for chest radiographic a-Se detectors at an applied electric field of $F = 10$ V/μm. The nominal exposure of $X = 300$ μR for chest radiography is used. The hole and electron lifetimes are assumed as 50 and 500 μs, respectively [59]. The photocurrent profile of the chest radiographic detectors is

similar to that of the mammographic detectors. However, the contribution of the electron current is higher in chest radiographic detectors than that in mammographic detectors because of more uniform carrier generation in chest radiographic detectors over a longer photoconductor length. The magnitude of the total photocurrent is higher in mammographic detectors compared to chest radiographic detector at the same electric field and temperature.
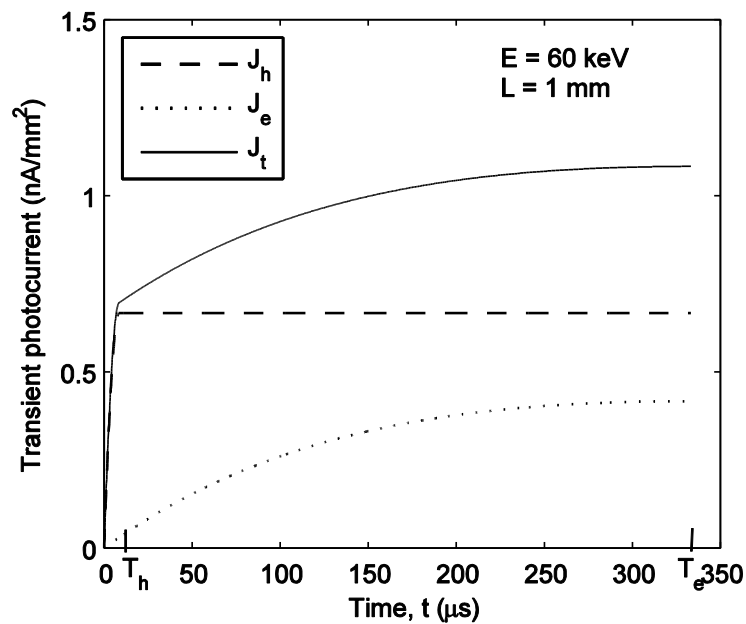


Figure 4.6: Transient photocurrent versus time in a-Se chest radiographic detectors at room temperature and electric field of 10 V/μm. The dotted, dashed and solid lines represent the electron, hole and total current respectively [58].

## 4.2.3 Transient Photocurrent Decay after X-ray Excitation

The transient photocurrent decay after turning off the exposure is also analysed. Figure 4.7 and 4.8 show the transient photocurrent decay after turning off the exposure as a function of time, $t'$, in a-Se mammographic and chest radiographic detectors, respectively. All the parameters in Figs. 4.7 and 4.8 are the same as in Figs. 4.5 and 4.6, respectively. The initial faster photocurrent decay is due to the holes transport while the then slower decay is due to the electron transport.
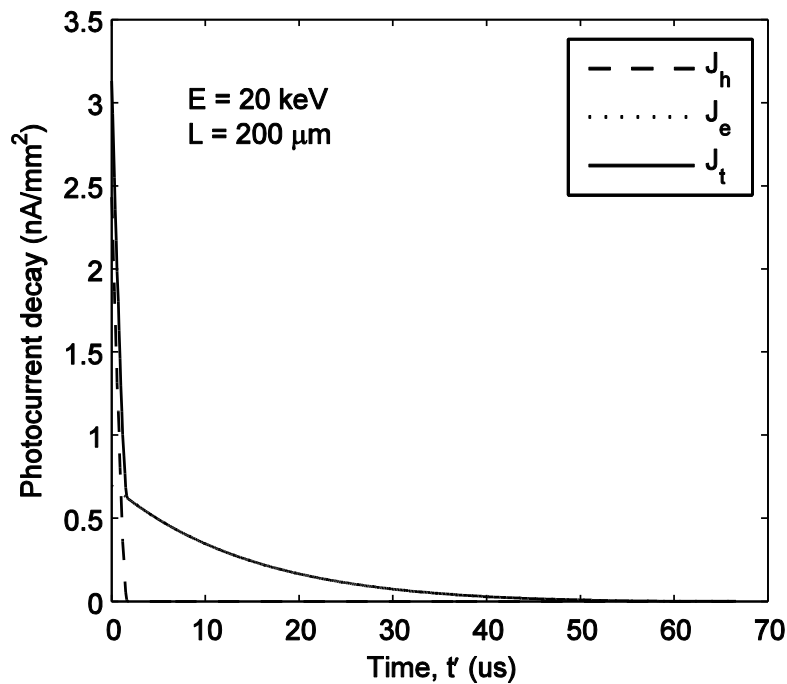


Figure 4.7: Photocurrent decay after turning off the exposure versus time in a-Se mammographic detectors at room temperature. The dotted, dashed and solid lines represents the electron, hole and total current respectively [58].
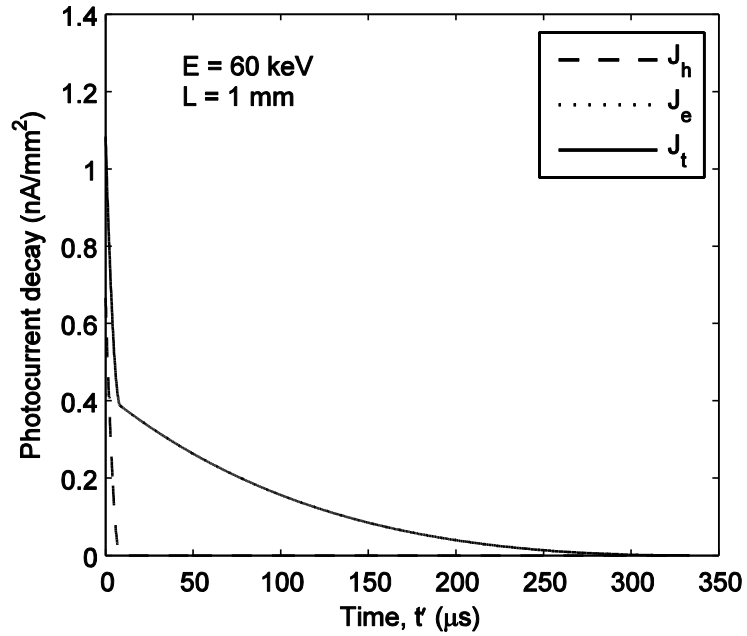
Figure 4.8: Photocurrent decay after turning off the exposure versus time in a-Se chest radiographic detectors at room temperature. The dotted, dashed and solid lines represent the electron, hole and total current respectively [58].

## 4.2.4 Residual Current

The residual current in the detector at different exposure intensities, ambient temperature and applied electric field for both chest radiographic and mammographic applications was also studied. The DOS in a-Se is constructed based on the following parameters: $g_h = g_e = 4 \times 10^{20}$ cm$^{-3}$eV$^{-1}$, $T = 275$ K, $v_0 = 10^{12}$ s$^{-1}$, $\varepsilon_r = 6.7$, $N_{h1} = N_{e1} = 10^{16}$ cm$^{-3}$eV$^{-1}$, $N_{h2} = N_{e2} = 10^{15}$ cm$^{-3}$eV$^{-1}$, $\Delta E_{h1} = \Delta E_{e1} = 0.1$ eV, $\Delta E_{h2} = \Delta E_{e2} = 0.2$ eV, $E_{h1} = 0.32$ eV, $E_{h2} = 0.9$ eV, $E_{e1} = 0.38$ eV, and $E_{e2} = 1.0$ eV. Unless otherwise stated these parameters are fixed for all the calculations in this paper.

Figures 4.9 and 4.10 show the residual current decay versus time at different exposures for chest radiography and mammography, respectively. The steady-state photocurrent density at $X$ = 300 μR in chest radiography (Fig. 4.9) is $1.1 \times 10^3$ pA/mm² whereas it is $4.2 \times 10^3$ pA/mm² at $X$ = 12 mR in mammography (Fig. 4.10).
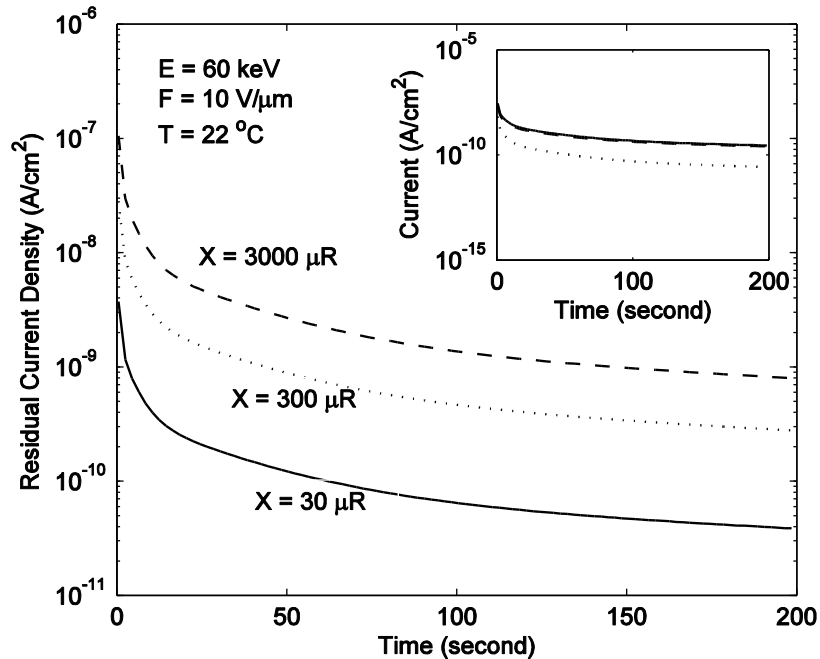


Figure 4.9: The residual current density versus time at various radiation exposures in chest radiographic detectors at room temperature and electric field of 10 V/μm. The dashed, dotted and solid lines in the inset figure are the electron, hole and total current densities, respectively [57].

The residual current increases with increasing exposure within the exposure range shown and it should reach a saturated value at extremely high exposure. Since the rate of carrier photogeneration is proportional to the radiation intensity incident on the detector, more charge carriers are available to be captured by localized states in the photoconductor at

higher exposures. The trapped carriers and thus the residual current get saturated when equilibrium is reached between the trapping and release events at extremely high exposures. The contributions of the hole and electron currents at the mean exposure intensity are shown as an inset graph for each of the imaging applications. The electron current makes a larger contribution to the total residual current due to the higher electron concentration in the photoconductor and lower mobility and hence the higher trapping rate of electrons.
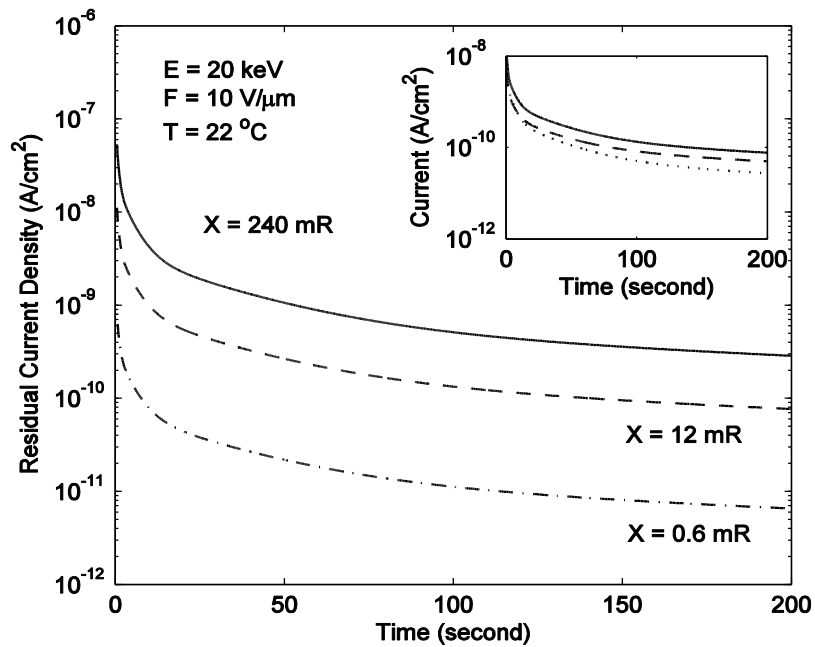


Figure 4.10: The residual current density versus time at various radiation exposures in mammographic detectors at room temperature and electric field of 10 V/μm. The dashed, dotted and solid lines in the inset figure are the electron, hole and total current densities, respectively [57].

The variation of residual current with ambient temperature for chest radiography at X = 300 μR and $F$ = 10 V/μm is shown in Figure 4.11. Increasing the ambient temperature facilitates the release of the captured carriers faster from the traps and the residual current increases with increasing the ambient temperature for the time scale shown. Similar results were obtained for mammographic detectors.
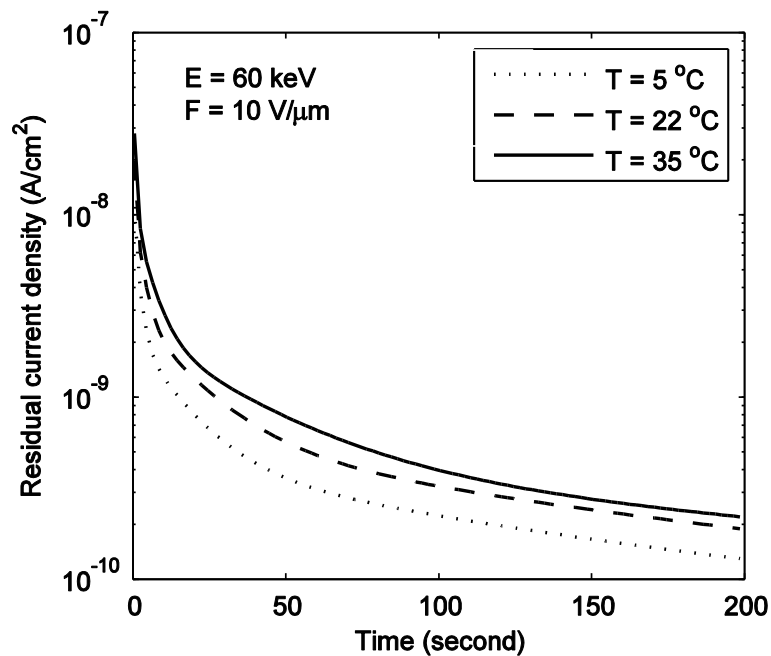


Figure 4.11: The residual current density versus time at various ambient temperatures in chest radiographic detectors for applied electric field of 10 V/μm [57].

The effect of the applied electric field on the residual current for a radiographic detector is shown in Figure 4.12. At higher electric field, fewer carriers are trapped in the localized states and the release of the trapped carries is enhanced by detrapping mechanisms such as

phonon-assisted tunneling. Therefore, the magnitude of residual current decreases as the electric field is increased. A similar result is also observed for mammographic detectors.
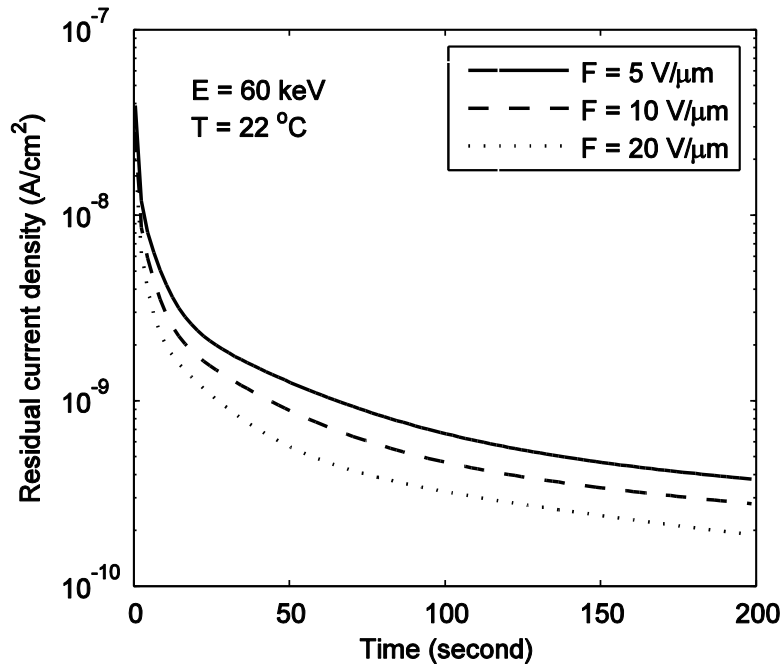


Figure 4.12: The residual current density versus time at various applied electric fields in chest radiographic detectors at room temperature [58].

## 4.2.5 Experimental Fit for X-ray Excitation

The theoretical model is verified by fitting with published experimental results. Loustaneau et al [60] investigated the lag signal properties in a-Se based X-ray detectors for mammographic applications. The percentage lag against time for three different exposures, i.e., 37 mR, 74 mR and 111 mR are shown in Figure 4.13. The symbols and lines (solid, dot and dash) represent experimental result and model fit to the experimental data, respectively.

The experimental data are extracted from Ref [60]. The amount of the defect states are varied to fit with the experimental data. The best fitted parameters are: $v_0 = 6 \times 10^{11}$ s$^{-1}$, $N_{h2} = N_{e2} = 10^{14}$ cm$^{-3}$eV$^{-1}$, $\Delta E_{h1} = \Delta E_{e1} = 0.146$ eV and $\Delta E_{h2} = \Delta E_{e2} = 0.07$ eV. All other parameters in Figure 4.13 are the same as in Figure 4.9. The fitted DOS parameters are within the experimental observation. The model shows good agreement with the experimental results within the limits of experimental error.
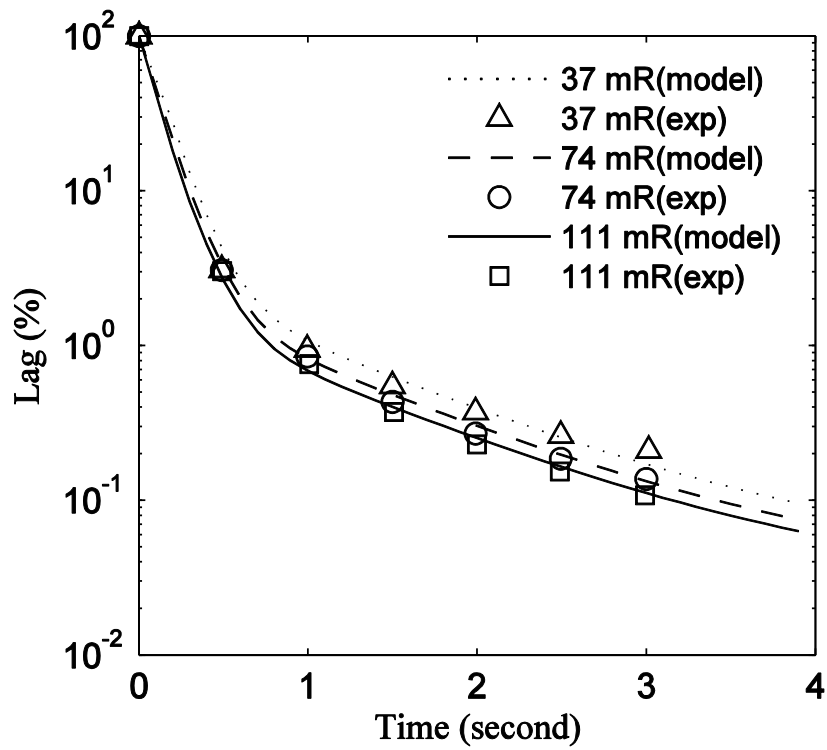


Figure 4.13: The percentage lag signal versus time at various exposures in a-Se mammographic detectors. The experimental data are extracted from Ref [60]

The theoretical model is also fitted with the experimental results in chest radiographic detectors as shown in Figure 4.14. The symbols and lines (sold, dot and dash) represent

experimental result and model fit to the experimental data, respectively. The experimental data are extracted from Ref [5]. The best fitted parameters are: $v_0 = 6 \times 10^{11}$ s$^{-1}$, $N_{h2} = N_{e2}$ $= 10^{14}$ cm$^{-3}$eV$^{-1}$, $\Delta E_{h1} = \Delta E_{e1} = 0.105$ eV and $\Delta E_{h2} = \Delta E_{e2} = 0.12$ eV. All other parameters in Figure 4.14 are the same as in Figure 4.9. As evident from Figures 4.13 & 4.14, the magnitude and duration of lag signal in chest radiographic detector is higher than that is mammographic detectors. The amount of trapped carriers in chest radiographic detectors is expected to be higher because of more photoconductor thickness and relatively uniform carrier generation.
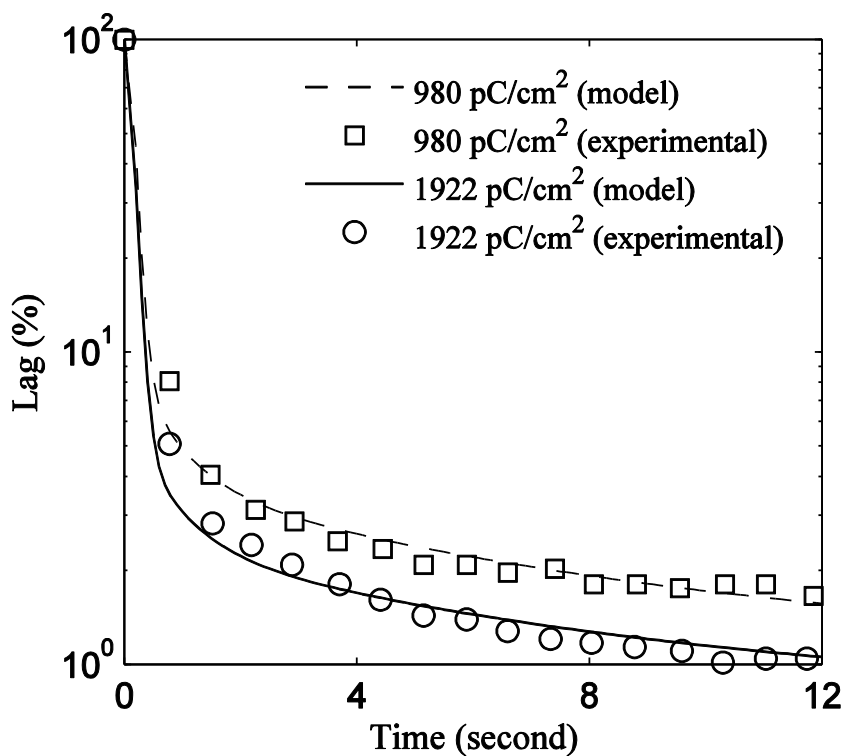


Figure 4.14: The percentage lag signal versus time at various exposures in a-Se chest radiographic detectors. The experimental data are extracted from Ref [5].

One interesting point to note from Figures 4.13 and 4.14 is that the percentage lag is smaller for higher exposure even though, as we saw previously, the residual current is higher. This occurs because the increase in the magnitude of the incoming signal at higher exposure is significantly greater than the increase in the residual current making the percentage lag smaller at high exposure.

## 4.3 Results for Optical Excitation

### 4.3.1 Carrier Concentration

For the optical model, the photoconductor thickness of the detector was taken to be $L = 15$ μm. The device was illuminated with blue light of wavelength, $\lambda = 468$ nm. The light intensity was calculated to be $I = 101$ μW/cm$^2$. For wavelength of 468 nm, the photon energy of the light is $E_{ph} = 2.6513$ eV, from which the linear attenuation α was found to be $1.55 \times 10^5$ cm$^{-1}$. The exposure time, $T_{ex}$, for each pulse is ~20 s. The room temperature effective hole drift mobility varies from ~0.12 cm$^2$/V-s to 0.85 cm$^2$/V-s for the field variation of 10 V/μm to 100 V/μm [61] and $\tau_h = 50$ μs is taken in all calculations. The DOS near valence band in a-Se is constructed based on the following parameters: $g_h = 4 \times 10^{20}$ cm$^{-3}$eV$^{-1}$, $T = 275$ K, $v_0 = 7 \times 10^{11}$ s$^{-1}$, $\varepsilon_r = 6.7$, $N_{h1} = 10^{16}$ cm$^{-3}$eV$^{-1}$, $\Delta E_{h1} = 0.1$ eV, $\Delta E_{h2} = 0.15$ eV, $E_{h1} = 0.27$ eV, and $E_{h2} = 0.85$ eV. Unless otherwise stated these parameters are fixed for all the calculations in this paper.

Figure 4.15 shows the variation of normalized hole and electron concentration along the photoconductor for different carrier lifetimes. The hole concentration rapidly increases in

magnitude near the surface and then maintains a uniform value. Varying the hole lifetime by one order of magnitude does not affect the carrier concentration significantly. The electron concentration, on the other hand, quickly becomes zero close to the surface and maintains a negligible value throughout the photoconductor for all electron lifetimes. As a result, the contribution of the electrons for the current was neglected in all calculations.
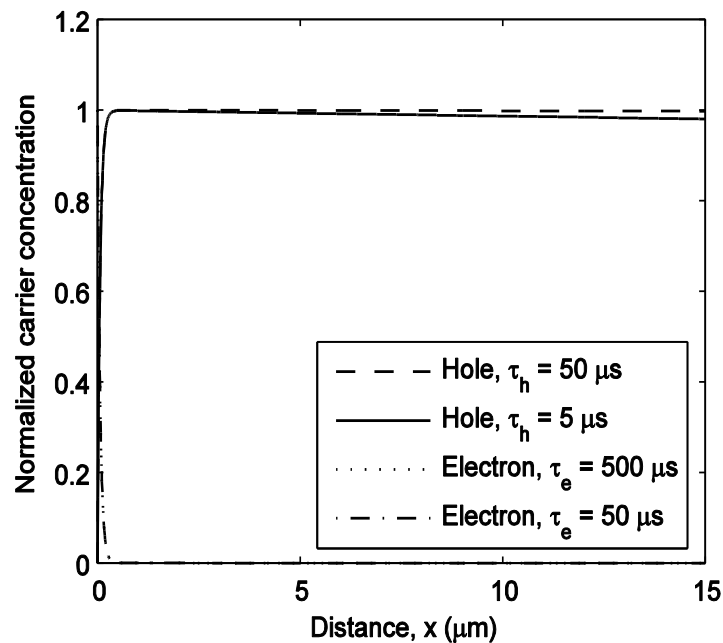


Figure 4.15: The normalized hole and electron concentration profiles for the optical irradiation of 468 nm wavelength.

## 4.3.2 Experimental Fit for Optical Excitation

The theoretical model was verified by comparing the results with experimental data obtained from Ref [6]. The results were plotted for two different exposure intensities 290

µW/cm² and 330 nW/cm² at room temperature and an applied electric field of $F = 30$ V/µm. The best fitting parameters were $v_0 = 9 \times 10^{11} s^{-1}$, $g_0 = 1 \times 10^{20}$ cm⁻³eV⁻¹, $E_{m1} = 0.27$ eV, $E_{m2} = 0.85$ eV, $\Delta E_{m1} = 0.1$, $\Delta E_{m2} = 0.2$, $N_{m1} = 1 \times 10^{16}$ cm⁻³eV⁻¹. For 290 µW/cm², $N_{m2} = 2.8 \times 10^{15}$ cm⁻³eV⁻¹ and for 330 nW/cm², $N_{m2} = 1.7 \times 10^{15}$ cm⁻³eV⁻¹ was considered. The solid and dashed lines show the theoretical results and the symbols represent the corresponding experimental findings. As seen in Figure 4.16, the two sets of data show good agreement within the limits of experimental error.
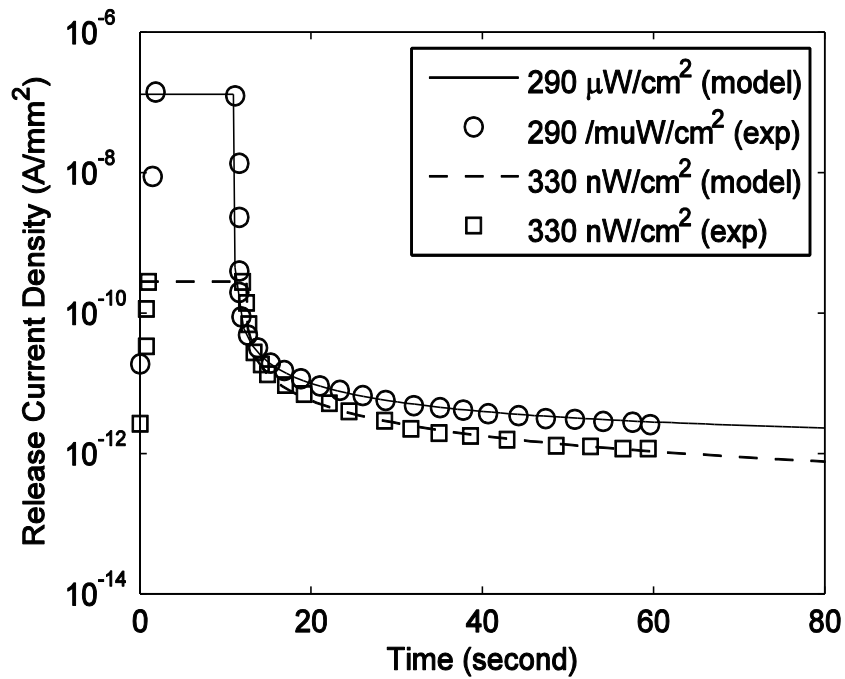


Figure 4.16: Decay current density vs time for optical exposure of 290 µW/cm² and 330 nW/cm². The experimental data were extracted from Ref [6].

## 4.4 Summary

In this chapter, the results obtained from the model for X-ray and optical excitation have been shown and discussed. The theoretical model was applied to a-Se photoconductor flat panel detector. For X-ray excitation, the model was analyzed for two common medical applications namely chest radiography and mammography. The distribution of the carrier concentration along the photoconductor length at various times for different carrier lifetimes has been plotted. The dependence of the lag signal on factors such as X-ray exposure, temperature and electric field has been analyzed. It was seen that the lag signal increases with increasing temperature and decreasing field. The electron and hole contribution to the total transient photocurrent and the photocurrent decay after removal of excitation has been plotted and discussed. The mathematical models were verified by comparing the theoretical results with published experimental data.

# CHAPTER 5: CONCLUSION AND FUTURE WORKS

## 5.1 Concluding Remarks

Flat-panel detectors (FPDs) are digital detectors that are widely used today for medical imaging applications such as general radiography and mammography. Amorphous Selenium (a-Se) is the only commercially viable photoconductor for direct FPDs. It is under development stage for indirect FPDs at extremely high fields with avalanche mode for low dose X-ray imaging.

A transient photocurrent is detected in the detector while it is exposed to X-rays (or visible light as the case may be). Although the photocurrent should return to zero once the exposure is turned off, an exponentially decaying current is observed in the detectors for a considerable amount of time even after the removal of the exposure. This is known as the residual current or lag signal. It is an undesirable phenomenon that leads to image artifacts such as image lag. It is caused by the structural defects found throughout the structure of a-Se. The defects appear as localized density-of-states (DOS) that captures the drifting holes and electrons in the photoconductor only to release them at a later time. The aim of this thesis was to develop a mathematical model to represent the entire current profile, which includes the photocurrent and residual current, of a-Se detectors for long X-ray as well as optical light pulses.

A physics-based model has been developed in this thesis. The expressions for free carrier concentration (both holes and electrons) were obtained by solving the continuity equation

with appropriate limits. The photocurrent was obtained based on the Ramo-Shockley current formula. The trapped carrier concentration and residual current was derived using the trapping rate equation. Since the linear attenuation coefficient of light is much higher than X-rays, light is mostly absorbed at the surface of the photoconductor simplifying the resulting photocurrent model. The expressions were used to analyze the carrier concentration, photo and residual current for different operational conditions such as temperature, electric field, exposure intensity and so on.

For X-ray exposure, the model was analyzed for two common medical applications namely chest radiography and mammography. It was observed that, for both applications, the residual current increases with increasing temperature but decreases with increasing electric field. The magnitude of the residual current was also found to be directly dependent on the X-ray exposure intensity. The electron current made a more significant contribution than the hole current for the total residual current detected for all observed cases. Interestingly, though, it was found that the percentage lag decreases with increasing exposure. In addition, the variation of the hole and electron concentration at different lifetimes for optical irradiation was plotted. The hole concentration remained practically uniform for one order of magnitude variation of the lifetime. The electron concentration reduced to zero very close to the surface and its effect was considered negligible. The validity of the X-ray and optical models were verified by fitting the theoretical results with published experimental data. The results showed good agreement within the limits of experimental error.

As mentioned earlier, this theoretical model will enhance our understanding of the physical mechanisms for photocurrent and lag signal in X-ray imaging detectors. And a better understanding of the phenomenon will help us develop ways to reduce its negative impact during imaging applications. For example, industries can now predict the lag signal in a detector and, accordingly, design readout circuits which will minimize image lag.

## 5.3 Future Work

The models in this thesis were developed for low to moderate X-ray and optical exposure in a-Se imaging detectors. As a result, the photogenerated carrier concentration was not high enough to perturb the electric field in the photoconductor. However, for very high exposure, the carrier concentration will be much greater which will make the electric field non-uniform across the photoconductor. Therefore, mathematical models considering spatially varying electric field in imaging detectors can be developed. In this case, a numerical model is necessary. Moreover, in this thesis, the models were only applied to amorphous selenium (a-Se) detectors. The model presented in this thesis can also be applied (with some modification) to other detectors such as polycrystalline $HgI_2$ and $PbO$ detectors or organic X-ray detectors.

# APPENDIX A – Justification of Uniform Electric Field

To develop the mathematical model, a uniform electric field is assumed across the photoconductor. The maximum change of the electric field $F$ for uniform carrier concentration $N'$ is

$$F = \frac{V}{L} - \frac{eN'L}{2\varepsilon_s}$$

where $V$ is the applied voltage, $L$ is the photoconductor length, $\varepsilon_s$ is the permittivity of a-Se, $e$ is the electronic charge and $N'$ is the carrier concentration. The carrier concentration is considered to be high enough to perturb the electric field when the variation in the electric field due to the charge distribution is $\geq 5\%$.

Let us consider a chest radiographic detector with $L = 1000$ µm and an applied electric field of 10 V/µm. For a 5% variation in the electric field, the formula becomes

$$5\% \, of \, 10V / \mu m = \frac{1.6 \times 10^{-19} \times N' \times 1000(\mu m)}{6.7 \times 8.85 \times 10^{-14}(F/m)}$$

$$\Rightarrow N' = 3.706 \times 10^{11} cm^{-3}$$

From the graphs shown in Section 4.2.1, it can be observed that the actual carrier concentration for this model is around two orders of magnitude lower than the calculated value of $N'$ above. In other words, the carrier concentration for the model is not high

enough to cause any significant field perturbation. Therefore, uniform electric field is a valid assumption.

# REFERENCES

[1] M. Bissonnette, M. Hansroul, E. Masson, S. Savard, S. Cadieux, P. Warmoes*, et al.*, "Digital breast tomosynthesis using an amorphous selenium flat panel detector," Proc SPIE, vol. 5745, pp. 529-540, 2005.

[2] P. R. Granfors and R. Aufrichtig, "Performance of a $41 \times 41$-cm2 amorphous silicon flat panel x-ray detector for radiographic imaging applications," *Medical physics,* vol. 27, pp. 1324-1331, 2000.

[3] E. Kotter and M. Langer, "Digital radiography with large-area flat-panel detectors," *European radiology,* vol. 12, pp. 2562-2570, 2002.

[4] S. Kasap, J. B. Frey, G. Belev, O. Tousignant, H. Mani, L. Laperriere*, et al.*, "Amorphous selenium and its alloys from early xeroradiography to high resolution X-ray image detectors and ultrasensitive imaging tubes," *Physica status solidi (b),* vol. 246, pp. 1794-1805, 2009.

[5] V. Loustauneau, M. Bissonnette, S. Cadieux, M. Hansroul, E. Masson, S. Savard*, et al.*, "Ghosting comparison for large-area selenium detectors suitable for mammography and general radiography," Proc SPIE, vol. 5368, pp. 162-169, 2004.

[6] S. Abbaszadeh, A. Tari, W. S. Wong, and K. S. Karim, "Enhanced Dark Current Suppression of Amorphous Selenium Detector With Use of IGZO Hole Blocking Layer," *IEEE Trans. Electron Devices,* vol. 61, pp. 3355-3357, 2014.

[7] S. A. Mahmood, M. Z. Kabir, O. Tousignant, and J. Greenspan, "Investigation of Ghosting Recovery Mechanisms in Selenium X-ray Detector Structures for Mammography," *IEEE Trans. Nuclear Science*, vol. 59, pp. 597-604, 2012.

[8] A. Walz-Flannigan, D. Magnuson, D. Erickson, and B. Schueler, "Artifacts in digital radiography," *American Journal of Roentgenology,* vol. 198, pp. 156-161, 2012.

[9] B. Fogal, R. E. Johanson, G. Belev, S. O'Leary, and S. Kasap, "X-ray induced effects in stabilized a-Se X-ray photoconductors," *Journal of non-crystalline solids,* vol. 299, pp. 993-997, 2002.

[10] E. Emelianova, M. Benkhedir, M. Brinza, and G. Adriaenssens, "Analysis of electron time-of-flight photocurrent data from a-Se," *Journal of applied physics,* vol. 99, pp. 083702-083702-4, 2006.

[11] S. Kasap, C. Koughia, J. Berashevich, R. Johanson, and A. Reznik, "Charge transport in pure and stabilized amorphous selenium: re-examination of the density of states distribution in the mobility gap and the role of defects," *Journal of Materials Science: Materials in Electronics,* pp. 1-15.

[12] T. Nagase and H. Naito, "Localized-state distributions in molecularly doped polymers determined from time-of-flight transient photocurrent," *Journal of Applied Physics,* vol. 88, pp. 252-259, 2000.

[13] M. Benkhedir, M. Brinza, and G. Adriaenssens, "Electronic density of states in amorphous selenium," *Journal of Physics: Condensed Matter,* vol. 16, p. S5253, 2004.

[14] A. W. Rau, L. Bakueva, and J. Rowlands, "The x-ray time of flight method for investigation of ghosting in amorphous selenium-based flat panel medical x-ray imagers," *Medical physics,* vol. 32, pp. 3160-3177, 2005.

[15] T.-T. Kuo, C.-M. Wu, H.-H. Lu, I. Chan, K. Wang, and K.-C. Leou, "Flexible x-ray imaging detector based on direct conversion in amorphous selenium," *Journal of Vacuum Science & Technology A,* vol. 32, p. 041507, 2014.

[16] D. Hunt, O. Tousignant, and J. Rowlands, "Evaluation of the imaging properties of an amorphous selenium based flat panel detector for digital fluoroscopy," *Medical physics,* vol. 31, pp. 1166-1175, 2004.

[17] http://www.analogic.com/products-medical-digital-mammography.htm

[18] M. Z. Kabir, M. Yunus, S. O. Kasap, O. Tousignant, H. Mani, and P. Gauthier, "Sensitivity of stabilized a-Se based X-ray photoconductors," *Current Applied Physics,* vol. 6, pp. 393-398, 2006.

[19] O. Bubon, G. DeCrescenzo, W. Zhao, Y. Ohkawa, K. Miyakawa, T. Matsubara*, et al.*, "Electroded avalanche amorphous selenium (a-Se) photosensor," *Current Applied Physics,* vol. 12, pp. 983-988, 2012.

[20] S. O. Kasap and J. Rowlands, "Direct-conversion flat-panel X-ray image sensors for digital radiography," *Proceedings of the IEEE,* vol. 90, pp. 591-604, 2002.

[21] J. G. Mainprize, D. C. Hunt, and M. J. Yaffe, "Direct conversion detectors: The effect of incomplete charge collection on detective quantum efficiency," *Medical physics,* vol. 29, pp. 976-990, 2002.

[22] W. Zhao, G. DeCrescenzo, S. O. Kasap, and J. Rowlands, "Ghosting caused by bulk charge trapping in direct conversion flat-panel detectors using amorphous selenium," *Medical physics,* vol. 32, pp. 488-500, 2005.

[23] S. A. Mahmood and M. Z. Kabir, "Dark current mechanisms in stabilized amorphous selenium based ni detectors for x-ray imaging applications," *Journal of Vacuum Science & Technology A,* vol. 29, p. 031603, 2011.

[24] N. Matsuura, W. Zhao, Z. Huang, and J. Rowlands, "Digital radiology using active matrix readout: amplified pixel detector array for fluoroscopy," *Medical physics,* vol. 26, pp. 672-681, 1999.

[25] K. S. Karim, A. Nathan, and J. A. Rowlands, "Amorphous silicon active pixel sensor readout circuit for digital imaging," *IEEE Trans. Electron Devices,* vol. 50, pp. 200-208, 2003.

[26] J. A. Rowlands and J. Yorkston, "Flat panel detectors for digital radiography," *Handbook of medical imaging,* vol. 1, pp. 223-328, 2000.

[27] B. Kolomiets and E. Lebedev, *Sov. Phys.-Solid State,* vol. 905, 1966.

[28] C. Haugen, S. Kasap, and J. Rowlands, "Charge transport and electron-hole-pair creation energy in stabilized a-Se x-ray photoconductors," *Journal of Physics D: Applied Physics,* vol. 32, p. 200, 1999.

[29] D. Adler, "Amorphous-semiconductor devices," *Scientific American,* vol. 236, pp. 36-48, 1977.

[30] D. Adler and E. J. Yoffa, "Localized electronic states in amorphous semiconductors," *Canadian Journal of Chemistry,* vol. 55, pp. 1920-1929, 1977.

[31] J. Berashevich, A. Mishchenko, and A. Reznik, "Two-Step Photoexcitation Mechanism in Amorphous Se," *Physical Review Applied,* vol. 1, p. 034008, 2014.

[32] G. Seynhaeve, R. Barclay, G. Adriaenssens, and J. Marshall, "Post-transit time-of-flight currents as a probe of the density of states in hydrogenated amorphous silicon," *Physical Review B,* vol. 39, p. 10196, 1989.

[33] M. Abkowitz, "Density of States in a-Se from Combined Analysis of Xerographic

Potentials and Transient Transport Data", *Philosophical Magazine Letters*, **58**, 53-57, 1988.

[34] S. O. Kasap and J. A. Rowlands, "Review X-ray photoconductors and stabilized a-Se for direct conversion digital flat-panel X-ray image-detectors," *Journal of materials science: materials in electronics,* vol. 11, pp. 179-198, 2000.

[35] M. F. Stone, W. Zhao, B. V. Jacak, P. O'Connor, B. Yu, and P. Rehak, "The x-ray sensitivity of amorphous selenium for mammography," *Medical physics,* vol. 29, pp. 319-324, 2002.

[36] I. Blevis, D. Hunt, and J. Rowlands, "Measurement of x-ray photogeneration in amorphous selenium," *Journal of applied physics,* vol. 85, pp. 7958-7963, 1999.

[37] S. O. Kasap, "X-ray sensitivity of photoconductors: application to stabilized a-Se," *Journal of Physics D: Applied Physics,* vol. 33, p. 2853, 2000.

[38] W. Que and J. Rowlands, "X-ray photogeneration in amorphous selenium: Geminate versus columnar recombination," *Physical Review B,* vol. 51, p. 10500, 1995.

[39] F. W. Schmidlin, "Theory of trap-controlled transient photocurrent," *Physical Review B,* vol. 16, p. 2362, 1977

[40] S. O. Kasap and C. Juhasz, "Time-of-flight drift mobility measurements on chlorine-doped amorphous selenium films," *Journal of Physics D: Applied Physics,* vol. 18, p. 703, 1985.

[41] H. Z. Song, G. Adriaenssens, E. Emelianova, and V. Arkhipov, "Distribution of gap states in amorphous selenium thin films," *Physical Review B,* vol. 59, p. 10607, 1999.

[42] R. Schwarz, "Dispersive transport in disordered semiconductors," *Journal of non-crystalline solids,* vol. 227, pp. 148-152, 1998.

[43] J. Berashevich, A. Mishchenko, and A. Reznik, "Two-Step Photoexcitation Mechanism in Amorphous Se," *Physical Review Applied,* vol. 1, p. 034008, 2014.

[44] M. Z. Kabir and S. A. Imam, "Determination of deep trapping states of the hole blocking layer in multilayer amorphous selenium X-ray detectors using transient dark current analysis 1," *Canadian Journal of Physics,* vol. 92, pp. 641-644, 2013.

[45] S. Ganichev, E. Ziemann, W. Prettl, I. Yassievich, A. Istratov, and E. Weber, "Distinction between the Poole-Frenkel and tunneling models of electric-field-stimulated carrier emission from deep levels in semiconductors," *Physical Review B,* vol. 61, p. 10361, 2000.

[46] J. Frenkel, "On pre-breakdown phenomena in insulators and electronic semi-conductors," *Physical Review,* vol. 54, p. 647, 1938.

[47] J. Hartke, "The Three-Dimensional Poole-Frenkel Effect," *Journal of Applied Physics,* vol. 39, pp. 4871-4873, 1968.

[48] A. Jonscher, "Electronic properties of amorphous dielectric films," *Thin solid films,* vol. 1, pp. 213-234, 1967.

[49] B. T. Polischuk, Z. Shukri, A. Legros, and H. Rougeot, "Selenium direct-converter structure for static and dynamic x-ray detection in medical imaging applications," Proc SPIE, vol. 3336, pp. 494-504, 1998.

[50] M. Z. Kabir, "Effects of charge carrier trapping on polycrystalline PbO x-ray imaging detectors," *Journal of Applied Physics,* vol. 104, p. 074506, 2008.

[51] J. M. Boone, "X-ray production, interaction, and detection in diagnostic imaging," *Handbook of medical imaging,* vol. 1, pp. 1-78, 2000.

[52] H. Naito, T. Iwai, M. Okuda, T. Matsuhita, and A. Sugimura, "Computer simulation study of tail-state distribution in amorphous selenium," *Journal of Non-Crystalline Solids,* vol. 114, pp. 112-114, 1989.

[53] M. Abkowitz, "Density of states in a-Se from combined analysis of xerographic potentials and transient transport data," *Philosophical magazine letters,* vol. 58, pp. 53-57, 1988.

[54] M. Z. Kabir, "Transient and steady-state dark current mechanisms in polycrystalline mercuric iodide X-ray imaging detectors," *Nuclear Instruments and Methods in Physics Research Section A: Accelerators, Spectrometers, Detectors and Associated Equipment,* vol. 736, pp. 156-160, 2014.

[55] M. Z. Kabir and N. Hijazi, "Temperature and field dependent effective hole mobility and impact ionization at extremely high fields in amorphous selenium," *Applied Physics Letters,* vol. 104, p. 192103, 2014.

[56] P. A. Martin, B. Streetman, and K. Hess, "Electric field enhanced emission from non-Coulombic traps in semiconductors," *Journal of Applied Physics,* vol. 52, pp. 7409-7415, 1981.

[57] S. Siddiuee, M. Z. Kabir, "Modeling of photocurrent and lag signals in amorphous selenium x-ray detectors," *Journal of Vacuum Science and Technolohy – A,* vol. 33, pp. 041514, 2015.

[58] S. Siddiquee and M. Z. Kabir, "Modeling of transient photocurrent in X-ray detectors: application to a-Se," *Physica Status Solidi* – under review.

[59] M. Z. Kabir, M. Yunus, and S. O. Kasap, "Dependence of x-ray sensitivity of direct conversion x-ray detectors on x-ray exposure and exposure history," Proc SPIE, vol. 5368, pp. 170-176, 2004.

[60] V. Loustauneau, M. Bissonnettea, S. Cadieuxa, M. Hansroula, E. Massona, and S. Savarda, "Imaging performance of a clinical selenium flat-panel detector for advanced applications in full-field digital mammography," Proc SPIE, vol. 5030, pp. 1011, 2003.

[61] S. Abbaszadeh, C. C. Scott, O. Bubon, A. Reznik, and K. S. Karim, "Enhanced detection efficiency of direct conversion x-ray detector using polyimide as hole-blocking layer," *Scientific reports*, vol. 3, pp.1, 2013.